First Alps-wide reconstruction of LGM glacial sediment transport enabled by GPU-accelerated particle tracking

Tancrède Pierre Marie Leger[1], Guillaume Jouvet[1], Sarah Kamleitner[1,2], Brandon David Finley[1], Maxime Bernard[1], Balthazar Allegri[1], Frédéric Herman[1], Andreas Vieli[2], Andreas Henz[2], Samuel Urs Nussbaumer[2]

[1]Institute of Earth Surface Dynamics, University of Lausanne, Lausanne, Switzerland

[2]Department of Geography, University of Zürich, Zürich, Switzerland

Correspondence: Tancrède P. M. Leger (tancrede.leger@unil.ch): personal address: tankleger@gmail.com

Abstract. Reconstructing the transport histories and provenances of glacial sediments and ice-contact deposits (e.g. tills, moraines) in formerly glaciated regions remains a major challenge, particularly at icefield-to ice-sheet scales and over multi-millennial timescales. Yet such reconstructions are central to key questions in Quaternary science, including estimates of past glacial erosion rates and sediment fluxes, the role of subglacial sediment storage in erosion buffering or the reconstruction of past ice-flow dynamics, ice divides, and transfluences. While numerical modelling can enable one to reproduce past glacial sediment transport via coupling glacier models with Lagrangian particle tracking, this becomes computationally unfeasible over large spatial domains and paleo timescales using traditional computing. As a result, no study to date has simulated glacial sediment transport using large particle numbers (tens of millions) across continental-scale icefields such as the European Alps during the Last Glacial Maximum (LGM): a pre-requisite given the ubiquitous nature of sediments in glacier systems. In this study, we overcome this limitation through a new coupling of 3D Lagrangian particle tracking with Graphics-Processing-Units (GPU)-accelerated, high-resolution glacier simulations based on the deep-learning-enhanced Instructed Glacier Model (IGM). Our approach unlocks the ice advection of tens of millions of particles at minimal additional computational cost, allowing simulations of glacial sediment transport across the European Alps over multi-millennial timescales (40-18 ka) and at an unprecedented spatial resolution of 300. In doing so, we produce the first Alps-wide modelling reconstruction of glacial sediment transport during the LGM, using process-based particle seeding schemes to represent both subglacial (e.g. abrasion, plucking) and supraglacial (e.g. rockfall, landslides) sediment sourcing. Results are analysed through complementary 'sink-to-source' (deposit provenance) and 'source-to-sink' (potential depositional pathways) analyses, enabling us to reconstruct the LGM glacial transport of numerous ice-contact deposits and surface lithologies across the Alps. We find that supraglacially sourced glacial sediments are typically eroded earlier, experience longer glacier residence times, and undergo greater cumulative ice-free exposure than those of subglacial origin, with implications for the interpretation of cosmogenic nuclide inheritance in glacial deposits. Our new coupled glacier-particle modelling framework opens avenues for quantitative model-data comparisons using glacial geomorphology and provides a powerful tool for reconstructing paleo ice dynamics, sediment provenance, and Quaternary glacial landscape evolution.

1 Introduction

In the early 1800s, pioneering naturalists argued certain sediments found in mountain forelands evidenced widespread past glacier expansions, an idea commonly known as the 'glacier theory' (e.g. Esmark, 1824; Venetz, 1830; Agassiz, 1840; Lyell, 1840). Their hypotheses were later validated by investigations characterizing deposits emplaced at the lateral, frontal, or subglacial margins of former glaciers, icefields, and ice sheets (Sugden & John, 1976). These so-called 'ice-contact deposits' include erratic boulders, lateral and terminal moraines, till units, drumlins, eskers, lineations, and various other glacio-depositional landforms (Evans & Benn, 2004). Over the last two centuries, glacial geologists have studied these features across formerly glaciated landscapes to reconstruct the extent, duration, style, and timing of past glacier advances and retreats (e.g. Penck & Brückner, 1909; Evans et al., 2006; Ehlers et al., 2011; Davies et al., 2012; Clark et al., 2022). In the European Alps, a long tradition of such work has focused on reconstructing Quaternary glaciations of the Alpine Ice Field (AIF) (e.g. Geikie, 1910; van Husen, 1997; Kelly et al., 2004; Preusser et al., 2010, 2011; Graf et al., 2015; Ivy-Ochs, 2015; 2022). Consequently, the processes of ice-contact sediment deposition and post-depositional disturbance are often well documented in many regions.

By contrast, the pre-depositional histories of ice-contact deposits are often poorly constrained. The inaccessibility and complexity of glacial sediment erosion/transport processes challenge empirical characterization in modern glacier systems, and even more so in paleo settings (Boulton, 1996). Field studies attempting to quantify pre-depositional histories in active glacier systems use techniques such as mineralogical provenance analyses (e.g. Herman et al., 2015), detrital and *in situ* low-temperature thermochronology (e.g. Enkelmann & Ehlers, 2015), terrestrial cosmogenic nuclide concentrations (e.g. Guillon et al., 2015), morainic soil material's fingerprinting analysis (e.g. Mohammadi et al., 2024), or luminescence rock surface burial dating (Margirier et al., 2025). However, these studies are rare, often limited to individual deposits or catchments, and difficult to extend to paleo glacier events. As a result, the provenance, erosion histories, transport distances, durations, and pathways of ice-contact deposits remain highly challenging to constrain at larger spatial and temporal scales.

Yet understanding glacial sediment erosion/transport history and their provenance is critical for multiple research questions. Such insights can, for instance, improve estimates of Quaternary glacial erosion rates and sediment fluxes, complementing studies of glaciofluvial sediment export dynamics (e.g. Koppes et al., 2015; Herman et al., 2015; Lane et al., 2017; Overeem et al., 2017; Delaney et al., 2023). They also inform mechanisms and timescales of debris cover and subglacial sediment storage, involved in bedrock shielding and erosion buffering (Delaney & Anderson, 2022). Pre-depositional sediment histories can also reveal past ice dynamics, including interactions with topography and the mechanisms of flow

76 convergence/divergence associated with tributary glaciers merging or separating during waxing and waning cycles of ice sheets or icefields (Jouvet et al., 2017). These reconstructions aid in identifying

78 former ice-flow regimes and the position or migration of ice divides, key to interpreting sedimentary archives of past ice-flow directionality (e.g. Hughes et al., 2010; Kamleitner et al., 2024) and to mapping

80 former ice transfluences (e.g. Reitner et al., 2010). Moreover, knowing whether a deposit reached glacier ice supraglacially or subglacially, and its glacial transport history, supports the application of

82 geochronological methods (e.g. cosmogenic exposure or luminescence dating), where prior exposure to sunlight or the atmosphere can affect age interpretations (e.g. Heyman et al., 2011). Quantifying glacial

84 sediment routing and export in formerly glaciated landscapes is also crucial to inform industries for instance concerned with aggregate resources or the geological disposal of nuclear waste (e.g. Fischer et

86 al., 2015; 2021). Lastly, tracking the transport history of iconic glacial erratics, some of which have cultural significance (Reynard, 2004; Coutterand, 2018), offers an opportunity to bridge scientific

88 understanding with public engagement. Thus, while it represents a substantial challenge, characterizing the pre-depositional history of glacial sediments and ice-contact deposits yields widespread implications

90 for numerous research fields.

92 Numerical modelling offers a means to address the above knowledge gaps by generating spatially distributed, time-evolving estimates of glacial sediment transport which can be compared against

94 empirical point data (e.g. Veness et al., 2025). A robust and established method consists in coupling a glacier evolution model with Lagrangian particle tracking to simulate the time-transient advection of

96 sediment-like particles by ice-flow (e.g. Rybak & Huybrechts, 2003; Rowan et al., 2015; Bernard et al., 2020; Scherler & Egholm, 2020). When modelled glacier geometries are somewhat consistent with

98 empirical evidence, and when particle seeding is parameterised to mimic real sediment erosion processes, this method can produce first-order estimates of glacial sediment transport pathways (Margirier et al.,

100 2025). However, no studies have yet coupled Lagrangian tracking of large particle numbers (>10^6) to multi-millennial-scale simulations of past Alpine Ice Field (AIF) glaciations. This is largely due to two

102 constraints. First, previous AIF simulations exhibited potent mismatches in ice thickness compared to field data, limiting confidence in inferred ice-flow dynamics (Mey et al., 2016; Seguinot et al., 2018; Jouvet et

104 al., 2023). Second, standard numerical approaches impose a high computational cost and high memory requirement when conducting Lagrangian tracking of large particle numbers: i.e. tens to hundreds of

106 millions of particles. Given the highly ubiquitous nature of sediments in glacier systems, such high particle numbers are essential if one wants to realistically depict some of the natural processes involved (Rowan

108 et al., 2015). Consequently, no studies to date have simulated glacial sediment transport using large particle numbers across continental-scale icefields like the AIF at any timescale, let alone over thousands of years.

110
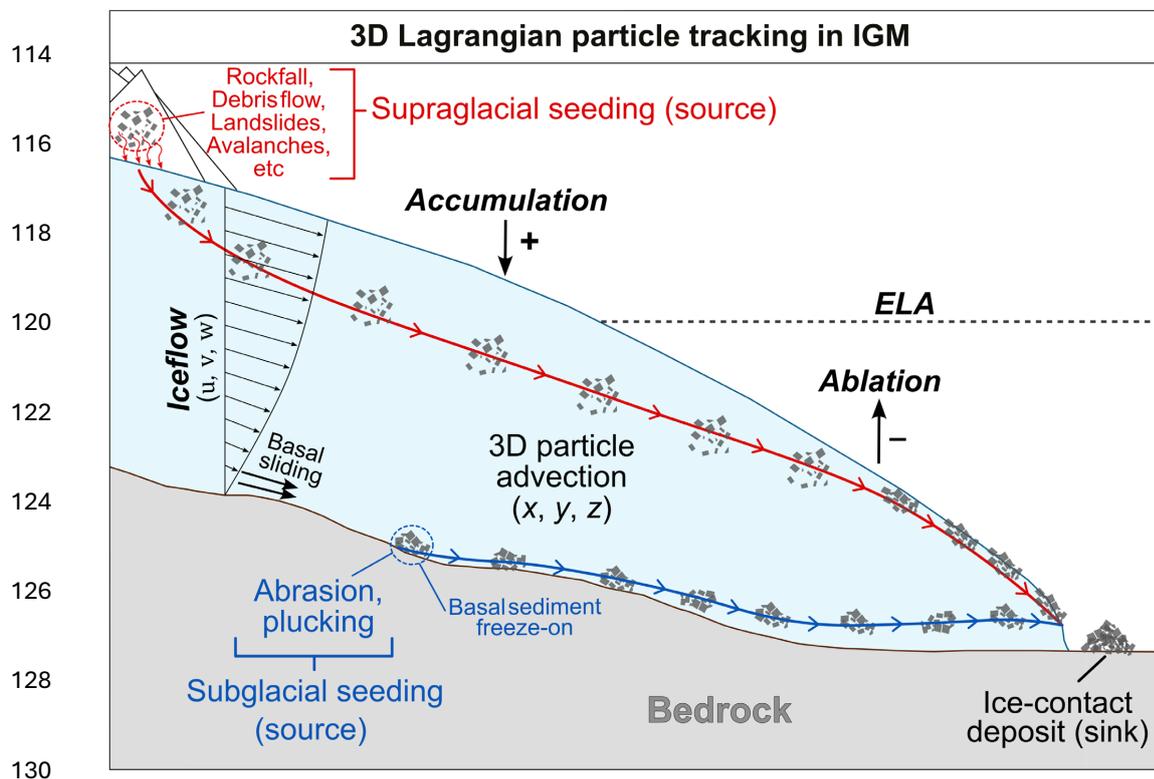
112

Figure 1. Simplified schematic diagram illustrating the Graphics-Processing-Units (GPU) - based, 3D Lagrangian particle advection scheme of both supraglacially seeded (red) and subglacially seeded (blue) particles coupled with our Instructed Glacier Model (IGM) setup and implemented in this study. 'ELA' stands for 'Equilibrium Line Altitude'.

Here we show that these bottlenecks can be overcome. Leger et al. (2025) produced an ensemble of 100

152 high-resolution (300 m) simulations of the AIF during the Last Glacial Maximum (LGM), whose best-
performing simulations improved model-data agreement in both ice thickness and extent compared to

154 previous efforts (e.g. Seguinot et al., 2018; Jouvet et al., 2023). These advances were enabled by the
Instructed Glacier Model (IGM), a high-order, thermo-mechanically coupled glacier evolution model

156 (Jouvet et al., 2021; Jouvet & Cordonnier, 2023). IGM leverages physics-informed machine learning and
computation on Graphics Processing Units (GPU) to reduce the computational cost of traditional glacier

158 modelling by several orders of magnitude. Here we show that IGM's novel GPU-based architecture also
enables efficient parallelization of Lagrangian particle tracking, permitting to couple the advection of

160 millions of particles within our AIF model framework at minimal additional cost (see Results section) and
consequently track the glacial-transport trajectories of individual particles from their location of origin

162 (the source) to their final deposition site (the sink).

164 To this end, we conduct a new set of Alps-wide simulations of the last glaciation of the European Alps
using the same data-consistent IGM setup as Leger et al. (2025) with the additional coupling of 3D

166 Lagrangian tracking of large particle numbers. Ultimately, we produce the first Alps-wide model estimates
of time-transient and 3D glacial sediment trajectories between 40 and 18 ka, the period bracketing the

168 LGM. We design a new particle advection module and seeding scheme that simulates both the subglacial
(e.g. via abrasion, plucking) and supraglacial (e.g. via rockfall, debris flow) origins of glacially transported

170 sediments (Fig. 1). By introducing this new method, we can simulate the complex glacial-transport
trajectories of LGM ice-contact deposits (e.g. terminal moraines) across the Alps at high spatial (300 m)

172 and temporal (10 yr) resolutions, and estimate their provenances, glacial transport time, erosion timing,
and cumulative ice-free time during their source-to-sink journey. With this experiment, we also model the

174 possible LGM source-to-sink trajectories of certain surface lithologies (i.e. sources) throughout the Alps,
which we subsequently compare against empirical data on LGM-dated erratics of known location and

176 lithology (e.g. Kamleitner et al., 2022).

178 The Alps-wide results of this study are presented below and use the form of figure catalogues and
trajectory shapefiles accessible via the Zenodo repository attached to this paper (link:

180 https://doi.org/10.5281/zenodo.18374156). They provide the means to compare our spatially distributed
modelling estimates against empirical evidence on, for instance, deposited LGM erratics and their

182 lithologies/provenance, former ice-flow direction during the LGM, documented ice transfluences, and
preserved post-retreat deposits and mapped moraines. We believe this first Alps-wide reconstruction of

184 LGM glacial sediment transport will prove useful to glacial geologists, geomorphologists,
sedimentologists, and industries studying ice-contact sediments related to the last glaciation of the

186 European Alps. This new ability to conduct coupled glacier-particle modelling over continental and multi-
millennial scales opens the door to new model-data comparisons which, in turn, can further improve the

188 accuracy of future AIF models. We provide examples showing how such model estimates can address empirical debates and raise new hypotheses that can be tested via future field campaigns. Finally, this

190 study provides a novel, computationally efficient modelling workflow which opens the possibility to produce high-resolution estimates of the erosion, transport, and deposition dynamics of glacial sediments

192 in numerous glaciated or formerly glaciated regions of the world.

194

2 Methods

196

2.1 Model setup

198

IGM is a thermo-mechanical 3D glacier evolution model enhanced with physics-informed deep learning

200 using a convolutional neural network emulator (Jouvet & Cordonnier, 2023) of the high-order 'Blatter-Pattyn' ice-flow solver (Blatter, 1995). In this study, we build on the results of Leger et al. (2025)

202 and use the exact same IGM model version (2.2.1), spatial resolution (300 m), input parameters, and forcings as used for their ensemble's (n=100) best-scoring simulation, i.e. simulation 37 (see Figs. 1, 6 in

204 Leger et al., 2025). We also run our simulations using the same GPU (Nvidia RTX 4090). In Leger et al. (2025), a perturbed-parameter ensemble of 100 simulations was performed, covering 35-18 ka at 300 m

206 spatial resolution across the European Alps, an order-of-magnitude improvement over previous 1-2 km models (Seguinot et al., 2018; Jouvet et al., 2023). Their model setup (and thus also ours) integrates

208 modules for ice-enthalpy (after Aschwanden et al., 2012), surface mass balance (after Calov & Greve, 2005), isostatic adjustment (after Wickert, 2015), and avalanching. The climate forcing was produced by

210 Russo et al. (2024) (also used by Jouvet et al., 2023), who conducted regional downscaling over Europe (2 km resolution) of global Earth-system model outputs using the Weather Research and Forecasting

212 model, providing gridded fields of temperature and precipitation for both the LGM (24 ka) and the pre-industrial era (1850 AD). A glacial index scheme generates continuous climate forcing interpolating these

214 two states using independent local proxy climate data that combines pollen and speleothem records (Fig. 2e in Leger et al., 2025; Luetscher et al., 2015; Duprat-Oualid et al., 2017). Basal sliding is parameterized

216 following a nonlinear Weertman friction condition (e.g. Schoof & Hewitt, 2013) with a sliding coefficient also influenced by enthalpy-driven basal meltwater content and elevation-dependent basal materials'

218 strength, following Bueler & van Pelt (2015) and the Mohr-Coulomb law (Cuffey & Paterson, 2010). For the bed topography, as in Leger et al. (2025)'s simulation 37, we use the digital elevation model from Mey

220 et al. (2016) which includes the removal of (1) present-day glacier thicknesses and lake depths, and (2) reconstructed present-day valley-fill sediment thicknesses in main overdeepenings throughout the Alps.

222 More detailed methods and model descriptions are presented in Leger et al. (2025).

224 Here, we employ this model setup to run two new simulations featuring the additional coupling of 3D

Lagrangian particle tracking. The first simulation is parameterised for subglacial particle seeding whilst

226 the second for supraglacial particle seeding (Fig. 1). We run all simulations between 40 and 18 ka, thus

starting 5 kyr earlier than the original setup. While Leger et al. (2025) showed that starting the simulation

228 before 35 ka had no noticeable impact on the modelled AIF geometry during the LGM (~24.8 ka in their

simulations), preliminary tests showed that it does affect the diversity of modelled particle trajectories

230 (more details in Results section).

232 **2.2 Particle seeding schemes**

234 For each model time step (every 0.01-0.04 yr) and domain cell (n = 6,030,036), we implement a set of

conditions to determine whether to 'seed' (i.e. create) a new particle or not. We exclusively focus on

236 estimating glacial sediment trajectories and transport statistics, and do not address the volumes of glacial

sediments, erosion, or deposits. Therefore, seeding of a new particle can be interpreted as the creation of

238 a new glacial 'sediment entity' within the glacier system, possibly ranging in size from grains to large

boulders. Note that throughout this paper, we use the terms 'glacial sediment' and 'glacial transport' to

240 describe all sediments that are transported by glacier ice, thus combining supraglacial, englacial, and

subglacial debris/transport. Below, we describe the set of conditions required for both subglacial seeding

242 and supraglacial seeding to occur in our model (Fig. 2).

244 The frequency and spatial distribution of subglacial seeding is here set to be a function of basal ice velocity,

as frequently observed (Humphrey & Raymond, 1994; Herman et al., 2015; Cook et al., 2020; Herman et

246 al., 2021). Here, we use the subglacial erosion law obtained by Koppes et al. (2015) from results on

sediment export volumes from several outlet glaciers of the Patagonian and Antarctic Peninsula icefields.

248 This non-linear erosion law assumes the erosion rate $\dot{e}$ is proportional to the sliding velocity u_s raised

to a power, using an erodibility constant $K_g = 5.2 \; x10^{-11}$ and a sliding velocity exponent of $l = 2.34$:

250

$$\dot{e} = K_g |u_s|^l \qquad\qquad 1)$$

252

We follow Seguinot & Delaney (2021) and assume glacier systems studied by Koppes et al. (2015) likely

254 yield similar dynamics to former outlet glaciers of the AIF during the LGM. Using this law, our model

computes an erosion rate and cumulative erosion over time for each grid cell (Fig. 2). Computed erosion

256 is not used to modify the bed topography dynamically but rather only as a quantitative proxy for particle

seeding. Once this artificial cumulative erosion reaches a certain threshold (here set to 4 cm), seeding

258 occurs and the erosion value is reset to 0, thus adding a new particle to the system (Fig. 2). This value (4

cm) is arbitrary and represents a parameter to control the total number of advected particles. To add

260 stochasticity to the modelled creation and freeze-on of subglacial sediment, seeding further requires

262 meeting a condition of time delay since last seeding occurred. This time delay is set to randomly vary between 10 and 60 yrs during the simulation following a uniform probability distribution (Fig. 2). Thus,

264 even though erosion is positively correlated to basal ice velocity, some randomness is here introduced in whether seeding will occur shortly or with some delay after the cumulative erosion threshold is reached.

266 Note that with this scheme, we do not model the glaciofluvial transport of subglacially eroded materials, as our model setup is not yet coupled to a subglacial hydrological-routing module. Instead, we exclusively

268 focus on subglacially eroded materials which freeze on and are subsequently advected by glacier ice (Alley et al., 1998). The limitations of this assumption are further mentioned in the Discussion section.

270 For supraglacial seeding, our scheme was conceived to simulate mechanisms generating supraglacial debris on glaciers, i.e. gravitational mass wasting events including rockfall, rock avalanches, debris flow,

272 avalanches, or landslides (Benn et al., 2012). We assume these events require both no (or little) ice cover and steep slopes to occur. We define all slopes steeper than 45° as susceptible to mass wasting (Fig. 2),

274 following recommendations from Fischer et al. (2012). However, our 300 m model resolution still smooths high-elevation peaks and steep slopes resulting in fewer locations >45° steep than in reality. To avoid this

276 bias, we use a higher-resolution digital elevation model (30 m resolution; Tadono et al., 2014) to produce a mask of pixels meeting a >45° slope condition. We consider all modelled ice that is <20 m thick and

278 located in pixels meeting the high-resolution >45° slope mask to be an artifact of our 300 m resolution, thus representing regions that would have no (or negligible) ice cover in reality. As a result, in our setup,

280 a given grid cell needs to both satisfy the >45° slope condition (in the high-resolution mask) and display modelled ice thickness <20 m, for supraglacial seeding to occur (Fig. 2).

282

As with subglacial seeding (see above), we introduce stochasticity in supraglacial debris production.

284 Firstly, supraglacial seeding only occurs when meeting a Boolean mask condition (True/False array) randomly shuffled for all domain cells (at every time step) with a True-value likelihood of 80%. Following

286 this, seeding also only occurs when meeting a time delay set to randomly vary between 20 and 160 yrs during the simulation (Fig. 2). All random sampling follows a uniform probability distribution. These

288 additional conditions separately add temporal and spatial randomness to supraglacial seeding, thus applying a probabilistic algorithm; common in mass-wasting event modelling (e.g. Champel et al., 2002).

290 Therefore, while gravitational mass wasting events are highly likely where/when the model features steep slopes (>45°) and a lack of ice cover, they are not necessarily going to occur at every time step and always

292 in the same locations (Fig. 2). Once seeded, particles are advected downslope following the steepest descent until slope angle <45°, or until reaching cells with modelled ice, in which case ice advection will

294 take over (Fig. 2).
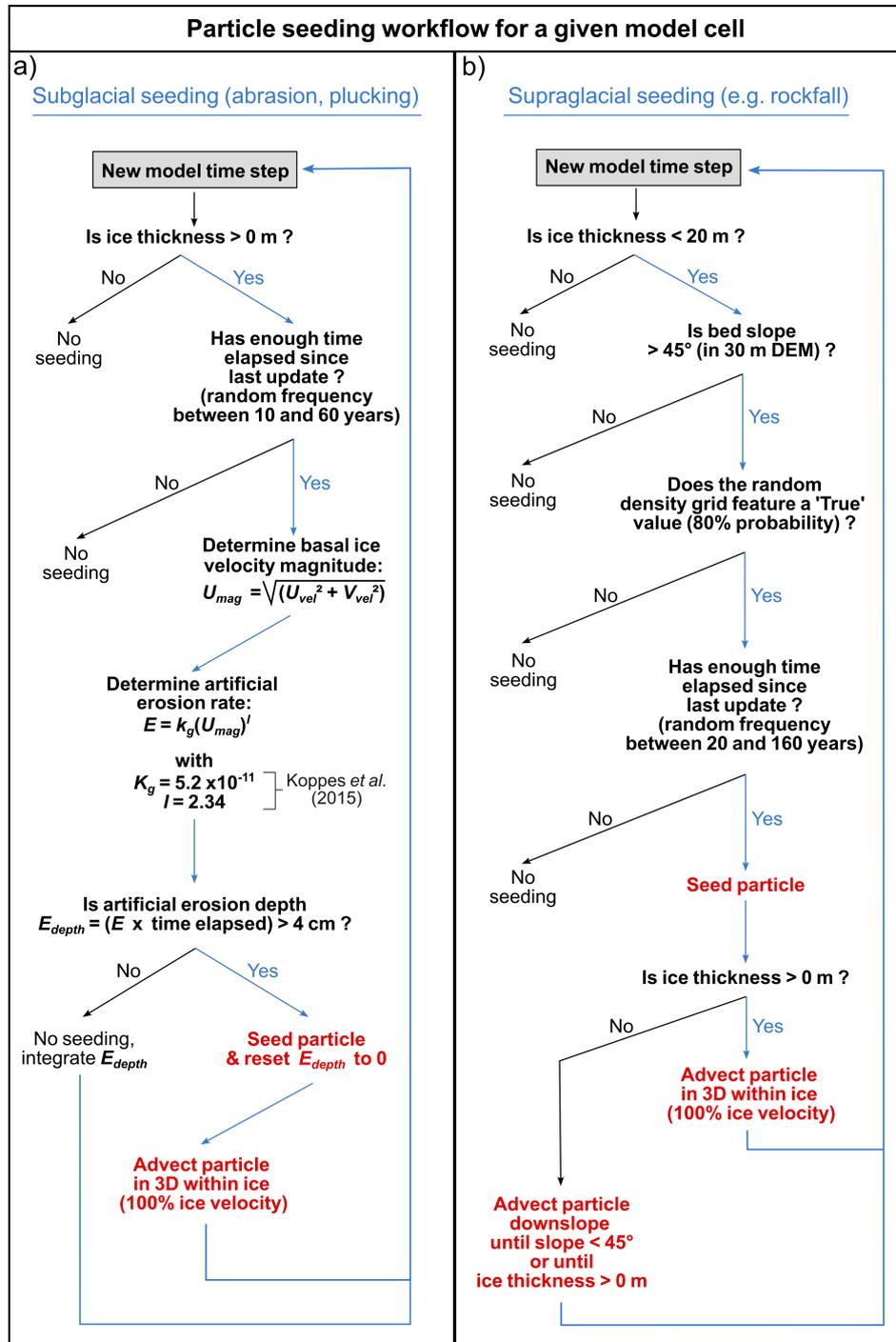
296

Figure 2. Decision chart indicating the model workflow specific to our particle seeding schemes for a given model cell (n = 6,030,036), and for the two cases of (a) subglacial seeding (abrasion, plucking) and (b) supraglacial seeding (e.g. rockfall, rock avalanche, debris flow, landslides, etc.). This chart summarizes the set of conditions and parameters applied to every model cell and at every model timestep (every 0.01-0.04 yr) during the simulation in order to seed, or not seed, a new particle within the model system.

344

2.3 Particle Lagrangian advection scheme

346

To track the movement of particles in 3D within the evolving glacier geometry, we use a Lagrangian

348   advection scheme which computes the space-time trajectory of particles created from seeding and resolves

the precise 3D positions of particles at sub-grid resolution. At each model timestep, IGM computes the 3D

350   ice-flow based on a high-order stress-balance model referred to as the 'Blatter-Pattyn' model (Blatter,

1995) and thus outputs a 3D velocity field. Each particle's horizontal (x, y) and vertical (z) positions are

352   thus updated according to ice velocity components u, v, w, respectively, integrated over a model timestep,

Δt, using an explicit Euler scheme.

354
$$x^{n+1} = x^n + \Delta t \cdot \bar{u}, \qquad\qquad 2)$$
$$y^{n+1} = y^n + \Delta t \cdot \bar{v},$$
356
$$z^{n+1} = z^n + \Delta t \cdot \bar{w},$$

358   where $\bar{u}, \bar{v}, \bar{w}$ represent the bilinearly interpolated horizontal and vertical velocities, respectively, at a

particle's current location (x^n, y^n). We ensure no particles artificially leave the ice column due to

360   numerical integration errors or transient velocity fluctuations by clipping their relative (normalized)

vertical positions to between 0 (bed) and 1 (ice surface). The bilinear interpolation for a scalar field f at a

362   sub-grid location (x, y) is computed using:

364
$$\bar{f}(x, y) = \sum_{i,j} f_{i,j} \cdot (1 - |x - i|) \cdot (1 - |y - j|) \qquad\qquad 3)$$

366   where the summation runs over the four grid nodes surrounding the particle's horizontal position, and the

weights $(1 - |x - i|)$ and $(1 - |y - j|)$ ensure a smooth linear interpolation based on the distances to

368   these nodes.

370   We assume all particles are advected at the velocity of the ice. The limitations of this assumption are

assessed in the Discussion section below. When a particle reaches the modelled ice margin and is

372   deposited, i.e. when ice thickness at its position becomes 0 m, it is prescribed the bed elevation. If local

slope is <45° this particle will remain stagnant (Fig. 2). If the modelled glacier re-advances and local ice

374   thickness is >0 m again, the particle gets re-entrained and 3D ice advection computations restart. We thus

assume that all temporarily deposited sediments freeze-on and get re-entrained by a re-advancing ice

376   margin. Although reality is more complex whereby former deposits can be overridden and survive younger

glacier advances, the process of re-entrainment is here considered to dominate (Cogez et al., 2018). This

378   assumption is supported by the general rarity, in formerly glaciated landscapes, of preserved older

moraines inboard of younger and more extensive terminal moraines (Gibbons et al., 1984).

380

Although particle positions are computed at every timestep (0.01-0.04 yr), they are saved every 10 model

382 years, which for our simulated timeframe (40-18 ka) generates 2200 data frames for each of the millions

of advected particles (20.5 million at maximum). The data saved for each particle include its x and y

384 coordinates, relative height in ice column, seeding year, and cumulative glacial transport time since

seeding. 10 years is the highest output frequency achieved while ensuring the particle database (~1.22 TB)

386 can be post-processed at a manageable computational cost. At that output temporal frequency, the post-

processing mapping of particle trajectories fully reflects the simulated ice-flow and particle advection in

388 most cases, except where modelled ice velocities are both high (e.g. >1000 m yr^{-1}) and towards highly

sinuous glacier motion (e.g. around valley bends), where mapping particle positions every 10 years can

390 result in unrealistically straight trajectories. This will however only impact the mapped trajectory towards

the bend and not reduce the accuracy of its modelled provenance nor destination.

392

2.4 Reconstructing glacial sediment trajectories

394

After running the glacier-particle coupled IGM simulations, we use the output database of particle

396 coordinates to map the time-transient trajectories of certain particles. This is conducted within the frame

of two analyses. The first one, hereafter referred to as the 'sink-to-source' analysis, aims at reconstructing

398 the provenance and glacial transport pathways of specific LGM terminal ice-contact deposits. The second

analysis, called 'source-to-sink', addresses the opposite question. Its objective is to estimate the possible

400 transport pathways and deposition locations of glacial sediments eroded from a pre-determined source.

402 The sink-to-source analysis consists finding all particles that end up within the area of a mapped deposit

at the end of the simulation (18 ka), after final glacier retreat, and trace back their glacial transport

404 trajectories. Although this can be achieved for any user-defined polygon, we focus on ice-contact deposits

located towards the terminal margins of main AIF outlet glaciers during the LGM (e.g. LGM moraines).

406 To follow a consistent methodology across the Alps, we map a series of 49 polygons (Fig. 3a) covering

the area between our most extensive time-independent modelled ice margin and the empirical LGM outline

408 of the AIF originally produced by Ehlers et al. (2011) and improved by several studies since (Gianotti et

al., 2008; 2015; Ravazzi et al., 2012; Monegato et al., 2017; Federici et al., 2017; Ivy-Ochs et al., 2018;

410 Braakhekke et al., 2020; Kamleitner et al., 2022; 2023; Ribolini et al., 2022). Tracing polygons over that

area between ensures olate all particles deposited at the LGM margins even where model-data fit in

412 ice extent is not perfect, which is still the case despite improvements relative to former AIF-wide LGM

models (Seguinot et al., 2018; Jouvet et al., 2023; see Fig. 4a in Leger et al., 2025).
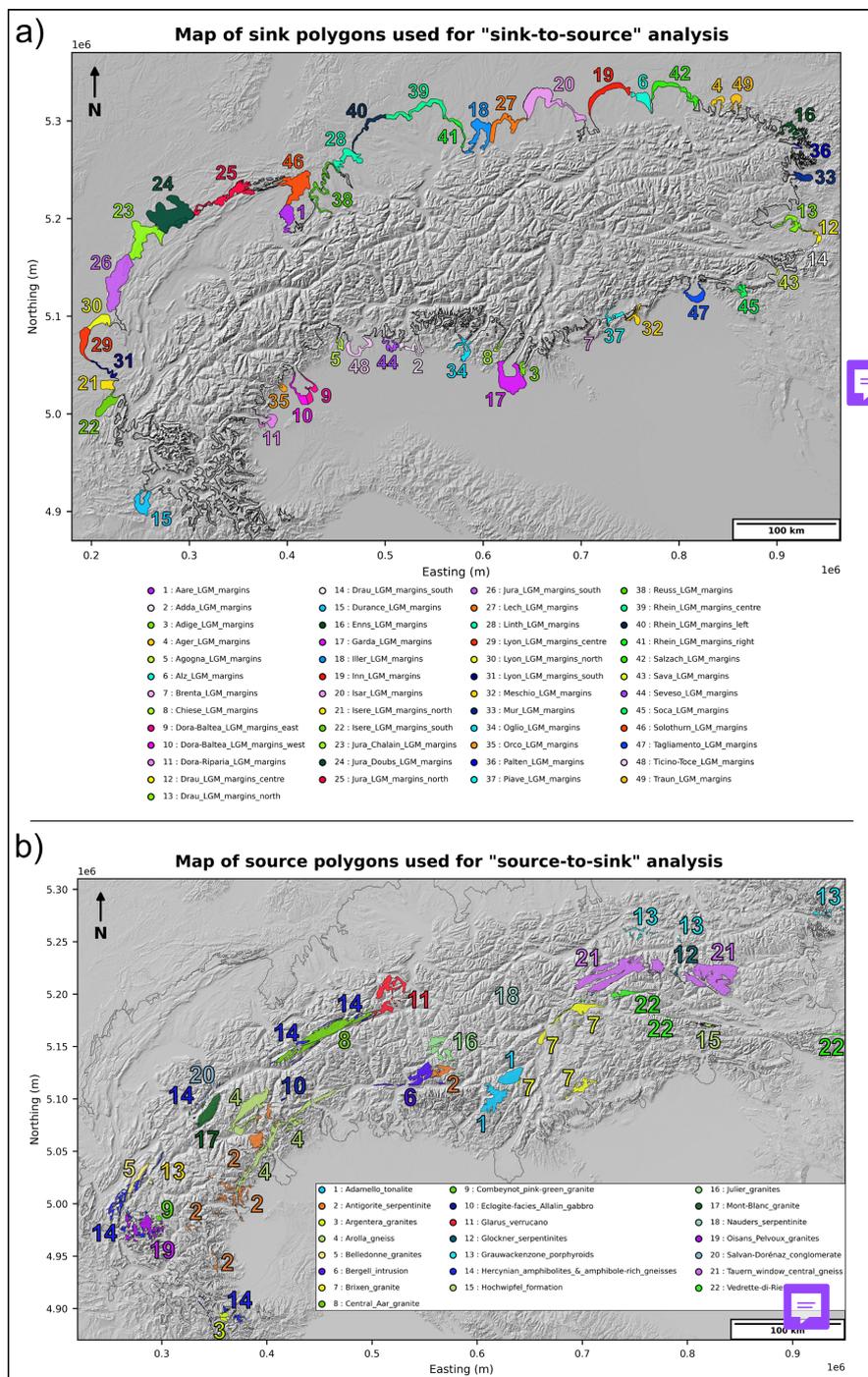
414

416

Figure 3. Maps of all sink and source polygons used for producing both catalogues of (a) sink-to-source and (b) source-to-sink analyses and their resulting particle trajectories. Sink polygons (a; n = 49) were selected and mapped to represent terminal ice-contact deposits for all major outlet glaciers of the Alpine Ice Field (AIF) during the Last Glacial Maximum (LGM), while source polygons (b; n = 22) were selected and mapped from geological data on surface outcrops for key lithologies across the Alps (more details in section 2.4). In this and all subsequent paper figures displaying geo-spatial data, X and Y coordinates are displayed as projected (unit: m) in the WGS 84 / UTM zone 32N (EPSG:32632) coordinate reference system.

12

456

Importantly, our 49 sink polygons (Fig. 3a) are not a precise map of terminal LGM ice-contact deposits preserved in the Alps. However, they are useful to produce a first-order estimation of possible LGM glacial trajectories for deposits located towards major outlet glacier margins, pre-erosion. Producing an Alps-wide, digital and open-access map of all preserved terminal ice-contact deposits dating to the LGM (e.g. Clark et al., 2018; Davies et al., 2020) has yet to be achieved in the Alps and is beyond the scope of this study. To estimate the relative contributions of various provenances to the total particle number found in a sink deposit, we divide our Alps-wide domain in 241 present-day hydrological catchments; obtained from the global HydroBASINS database (Lehner & Grill, 2013), and named based on catchment-specific river names (Figure S1). Our sink-to-source analysis produces a catalogue of modelled particle trajectories, estimated provenance fractions per basin, and statistics including glacial transport time and particle age (i.e. seeding year), for all particles found in each of the 49 sink polygons shown in Figure 3a. All results are produced separately for subglacial and supraglacial particle seeding, enabling us to compare the impacts of different sourcing mechanisms on glacial sediment transport histories and provenances.

470

For the source-to-sink analysis, we select sources that represent mapped outcrops of specific alpine surface lithologies, to estimate the glacial transport pathways of sediments from specific rock types between 40 and 18 ka, across the Alps. We focus on rock type as this enables us to compare modelled estimates against empirical data on ice-contact deposits (e.g. erratic boulders) of known lithologies and locations post-retreat (e.g. Braakhekke et al., 2020; Monegato et al., 2022). This requires identifying surface lithologies specific enough to be associated with mapped outcrops and uniquely recognisable through geological assessment of ice-contact deposits. The outcrops moreover need to cover a large-enough area for enough particle seeding to overlap them, given that a single grid cell is 90,000 m^2. To identify such lithologies, we use the open-access 1:500,000-scale geological map sheets 1 and 2 from the 'Structural model of Italy' (Bigi et al., 1990a; b). These maps present a relatively high spatial resolution, are easily accessible online and georeference-able, and provide a consistent naming convention of lithologies across the entire Alps. We also use geodata derived from the Geological Map of Austria 1:50.000 sheets 197 Kötschach and 198 Weißbriach for one extra lithology (i.e. the Hochwipfel formation) (Geologische Bundesanstalt Österreich, 2021a, b). We then isolate a subset of 22 surface lithologies referred to as our 'source polygons' (Fig. 3b). While these are not a comprehensive list satisfying the above criteria, they are spatially widespread and cover the main rock types described by investigations on LGM erratic boulders in the Alps. They include Mont-Blanc granite (Bussien Grosjean et al., 2018), Glarus Verrucano (Letsch et al., 2015), or Salvan-Dorénaz conglomerate (Capuzzo et al., 2003), for instance (Fig. 3b).

The source-to-sink analysis consists in finding all particles seeded within our 22 source polygons during the AIF simulations, and in mapping their glacial transport pathways. Due to existing mechanisms of sediment melt-out and lodgement at the ice-bed interface (Alley et al., 1997), we consider any location

13

along the resulting trajectories to be a possible destination for glacial sediment of the studied lithology.

494 Thus, the source-to-sink analysis produces a catalogue of maps displaying modelled trajectories of particles seeded within each of the 22 selected surface lithologies shown in Figure 3b. The maps are

496 produced for both subglacial and supraglacial particle seeding allowing for a direct comparison between the two.

498

Consequently, the main outputs of this study are the 'sink-to-source' and 'source-to-sink' analyses, i.e.

500 two catalogues of model results shared under the form of maps displaying source and sink particle trajectories, pie charts of deposit provenance fractions, histograms showing data from sink particles, and

502 polyline shapefile data for visualization in GIS software. These data are all accessible from the Zenodo repository attached to this paper (link: https://doi.org/10.5281/zenodo.18374156).

504

506 **3 Results**

508 **3.1 GPUs reduce the computational cost of particle tracking**

510 GPUs are particularly well-suited for particle-based numerical modelling, such as Lagrangian particle tracking, due to their architecture optimized for massively parallel execution of small, independent

512 computations, ideal for processing individual particles concurrently. This contrasts with traditional computing on Central Processing Units (CPU) which restricts the parallelization of such small operations

514 on much fewer cores. Consequently, GPU-accelerated algorithms for particle-based modelling have been extensively developed in fields as varied as fluid mechanics, graphics, or geosciences (e.g. Wang et al.,

516 2022; Aaron, 2023). In our specific application, we find that transferring all computation on the GPU makes 3D Lagrangian particle advection highly efficient, with a computational cost that remains small

518 even when tracking tens of millions of particles within a modelled glacier (Fig. 4).


520 To quantify this gain, we ran a test simulation over the majority of the European Alps and, after initializing an LGM Alpine Ice Field (AIF), seeded new particles in all grid cells of the glacier accumulation area

522 every two model years, thus quickly multiplying the total particle number. When operating on a single GPU (Nvidia RTX 4090), raising the number of particles from 0 to 50 million increases the mean cost of

524 computing their advection linearly between 0.02 and 0.1 seconds per timestep (Fig. 4). Even with 50 million particles in the system, the computational cost of particle tracking remains below 26% of the mean

526 cost (i.e. ~0.39 seconds per timestep) of all other IGM processes and modules in our Alps-wide simulation of the LGM at 300 m resolution. When running the same test using multiple CPUs instead, the mean costs

528 of tracking 50 million particles reach approximately 26 and 5.5 seconds per timestep using 12 and 60 CPU threads, respectively (Fig. 4). These computational costs are between 274 and 55 times greater than those

obtained with a single GPU, respectively. For 10 million advected particles, the costs are still 200 and 42 times greater than with the GPU, respectively. This shows that when using any traditional CPU-based glacier evolution model, coupling Lagrangian tracking of large particle numbers ($>10^7$) would substantially increase the simulation's computational cost. The alternative of accurately computing particle trajectories using post-processing only (after simulations are run), although not computationally restrictive, would be made impossible by the data volume of transient 3D velocity fields that would need to be saved at every time step (0.01-0.04 yr), which in our case would quickly exceed the hundreds of Terabytes. Contrastingly, when using IGM and a GPU-based approach, 3D particle tracking of large particle numbers can be coupled to simulations with only a small additional cost relative to the ice-flow model (Fig. 4). This enables us to run, for the first time, IGM simulations at high (300 m) spatial resolutions with millions of particles tracked over Alps-wide and multi-millennial scales, an experiment that would be unfeasible using traditional CPU-based computing.
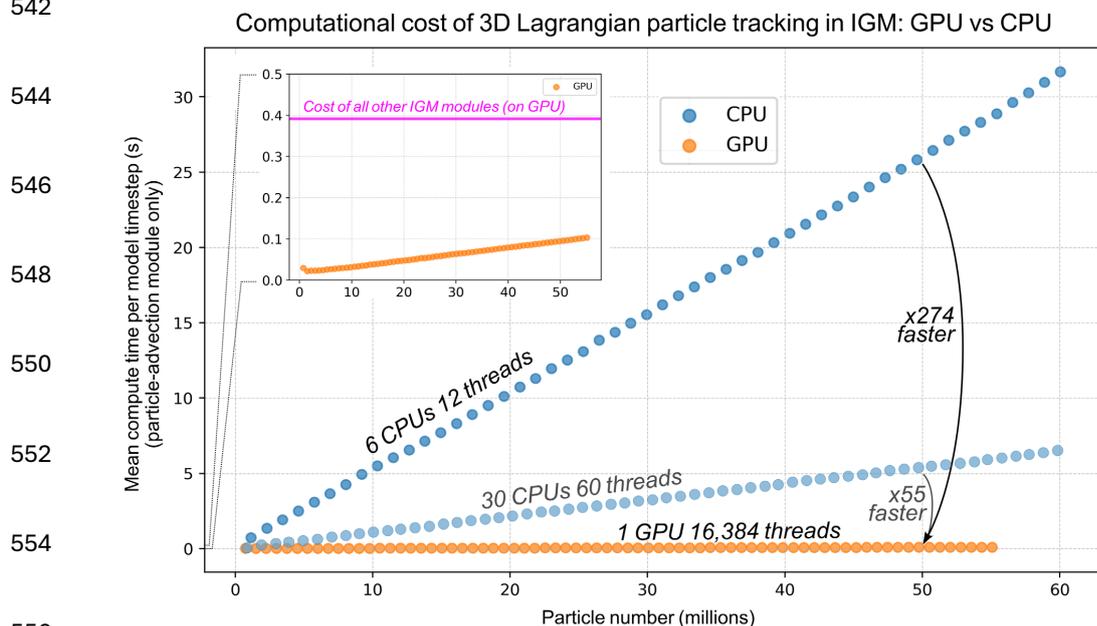
Figure 4. Mean computational time/cost (in seconds) of computing the Lagrangian 3D advection of particles in ice during a single model timestep of our Alpine-Ice-Field simulations with the Instructed Glacier Model (IGM), as a function of particle number. The data shown here allows one to compare the computational cost of Lagrangian particle tracking on a single GPU (orange dots; Nvidia RTX 4090) relative to computing it on multiple CPU cores (blue dots; Intel(R) Xeon(R) CPU E5-2620 v3). The difference between blue and orange dotted lines highlights the significant computational gain of parallelizing particle advection operations on the GPU. The intermediate line of blue dots (30 CPUs, 60 threads) is shown with slight transparency as numbers were calculated assuming linear proportionality to the real computational costs obtained with a 6 CPU (12 threads) setup. The inset graph changes the Y scale and zooms inside compute time values <0.5 seconds, allowing one to visualize the linear increase in cost with increasing numbers of advected particles when using the single GPU (otherwise invisible). The inset also compares this particle-module cost against the average computational cost (~0.39 s: pink line) of a single model timestep when combining all other GPU-based IGM modules used when running the Alps-wide 300 m best-fit simulation of Leger et al. (2025): i.e. the same simulation we re-run in this study.

572

3.2 Alps-wide patterns of glacial sediment sourcing

574

Our coupled glacier-particle simulations output a database of 3D particle coordinates and other statistics

576 from the moment of seeding until the end of the glacier simulation (i.e. 18 ka). Thus, for both simulations

with subglacial and supraglacial particle seeding, a map of seeding locations for each of the ~20.5 million

578 advected particles can be produced. To visualize the spatial heterogeneity of particle seeding, we transform

the seeding location data into normalized seeding density maps (Fig. 5). In Figure 5, bright colours

580 (normalized density closer to 1) show regions with relatively more particle seeding events during the

simulations. For subglacial seeding, these regions are associated with high basal ice velocities modelled

582 during extended periods of the simulation, spanning 40-18 ka. These can be interpreted as likely to produce

the largest volumes of glacial sediments of subglacial origin (e.g. abrasion and plucking) during the LGM.

584 Potent subglacial sediment sourcing regions include the Rhône valley between Montreux and Sion

(Switzerland), the Dora Baltea valley between Aosta and Ivrea (Italy), the Romanche valley between Le

586 Bourg-d'Oisans and Grenoble (France), or the Rhein valley between Domat/Ems (Switzerland) and

Bregenz (Austria), for instance (Fig. 5a).

588

For supraglacial seeding, regions of high seeding densities are those presenting steep topographies (>45°)

590 and ice-free conditions (or thin ice cover <20 m) during extended time-periods of the simulation. These

regions also need to be near dynamic modelled glaciers for seeded particles to eventually get transported

592 by glacier ice. These regions are interpreted as likely to have produced the largest volumes of supraglacial

sediments (e.g. from rockfall, debris flow, landslides, avalanches) during the LGM. Our results suggest

594 that high supraglacial sediment sourcing regions are widespread (Fig. 5b) but include, for instance, the

Écrins Massif (France), the Lepontine Alps (Switzerland), the Dolomiti Bellunesi Massif (Italy), the

596 Triglav Massif (Slovenia), or the Bernese Alps (Switzerland). During the LGM, these regions are most

concentrated within a narrow band located towards the northern and southern peripheries of the alpine arc,

598 where high topographies (> 2500 m a.s.l.) combined with thin/no ice cover maximize the likelihood of

nunatak occurrence (Fig. 5b). Contrastingly, supraglacial sediment sourcing is lower further towards the

600 Alps' interior, where the model produces greater ice thicknesses and topographic ice covers for extended
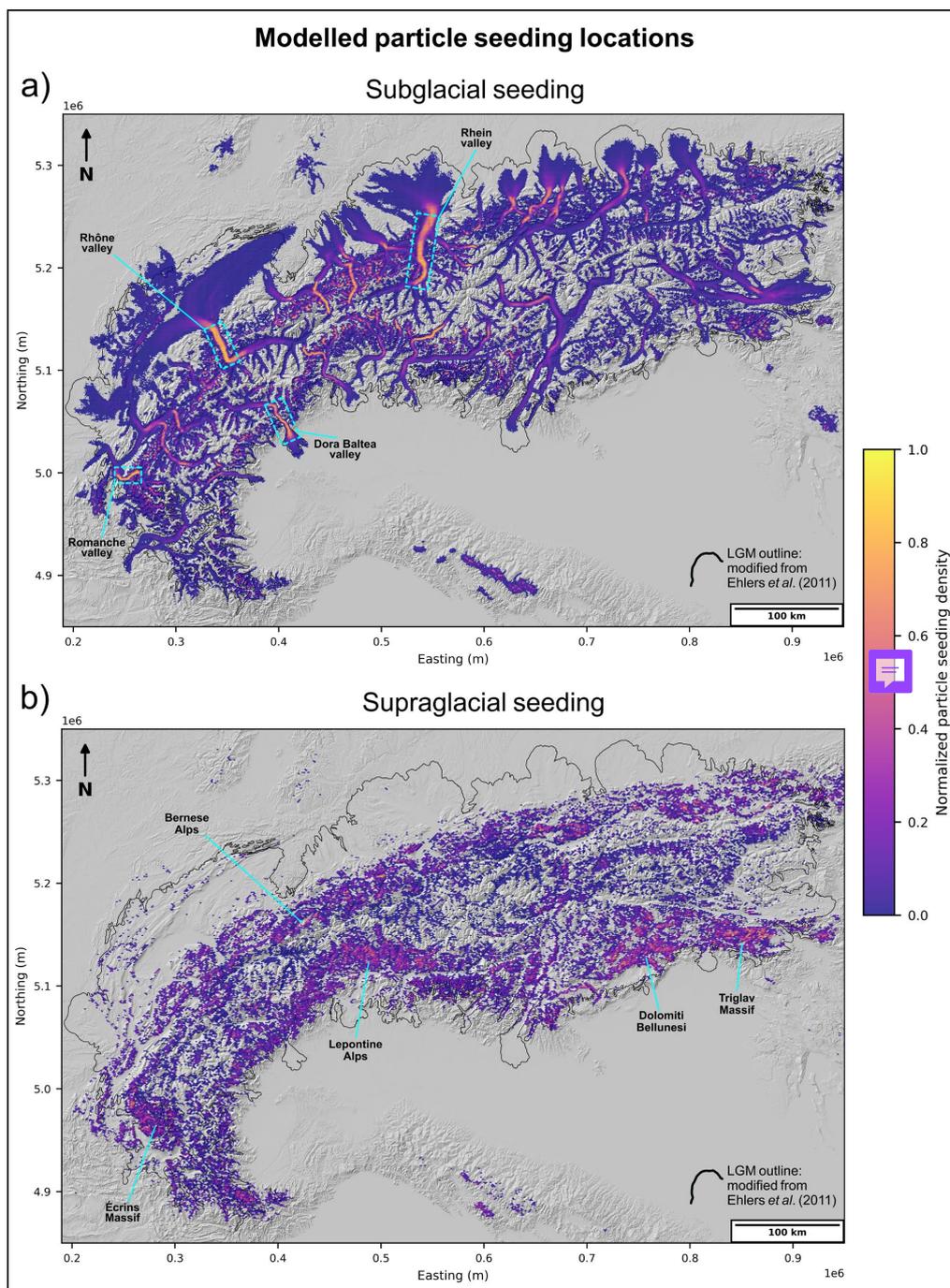
periods, thus reducing nunatak occurrence.

602

604

606

Figure 5. Maps showing the seeding locations of all modelled particles (~20.5 million at maximum) in both simulations with (a) subglacial and (b) supraglacial particle seeding. The maps are divided into small hexagons in which the total number of seeded particles is computed. Hexagons are colored based on this total number normalized across the entire dataset, resulting in a density map of particle seeding locations, with brighter yellow colors indicating relatively more seeding, and darker purple colors indicating relatively less seeding. A lack of colors (grey hillshade background) indicates no particle seeding occurred at any time during simulations.

3.3 The sink-to-source analysis and catalogue

With the sink-to-source analysis, we produce a catalogue of modelled time-transient trajectories for terminal LGM ice-contact deposits mapped across the Alps, hereafter referred to as our 'sinks' (see section 2.4). Sink-to-source trajectories reveal the modelled pathways of ice-advected particles ending up within these sinks after final glacier retreat. For each sink polygon mapped (n = 49; Fig. 3a), we provide a high-resolution map of particle trajectories, along with an estimation of particle provenance fraction. For each sink and particle in this sink, we also produce statistics on total particle glacial transport distance, cumulative glacial transport time, cumulative time in ice-free conditions during source-to-sink journey, and seeding year (i.e. timing of erosion). These data are produced for both cases of subglacial and supraglacial seeding, enabling us to quantify differences in glacial transport dynamics between the two. We consider the sink-to-source catalogue to be a main result of this study and encourage readers to download it from the Zenodo repository attached to this paper (link: https://doi.org/10.5281/zenodo.18374156). All particle trajectory data for each seeding type and sink are also available as polyline shapefiles for visualization in GIS software.

3.3.1 A sink-to-source case study: the Inn glacier LGM margins

As a case study, we here describe the results of our sink-to-source analysis for a single ice-contact deposit, i.e. the Inn glacier LGM margins (sink 19; Fig. 6). We chose this outlet glacier as its modelled ice-flow during the LGM originates from a large variety of catchments, produces numerous transfluences, has been the subject of several studies (e.g. Reitner, 2007; van Husen, 1997), and produces a good ice-extent fit during maximum expansion with empirical data (see Fig. 1a in Leger et al., 2025). In our subglacial and supraglacial seeding simulations, totals of 53,797 and 36,945 particles end up within this ice-contact deposit, respectively (Fig. 6). The sink particles originate from 15 (for subglacial seeding) and 12 (for supraglacial seeding) different hydrological basins. Our modelling suggests the basin contributing the most ice-contact sediments of subglacial origin is the Inn-Simsee basin (basin 44; Figure S1), with an estimated provenance fraction of 42.5% (Fig. 6). For supraglacial seeding, the distribution of provenance fractions is different. The basin estimated to provide the most sediments of supraglacial origin is the Ziller basin (basin 191; Figure S1), although its provenance fraction (32%) is tied with the Alz-Traun basin (basin 63, 29.5%). On average, our modelling suggests that ice-contact deposits of the LGM Inn glacier margins spent 3,021 ± 4, yrs (median ± interquartile range) in glacier ice for those of subglacial origin. This median number is approximately twice greater for ice-contact deposits of supraglacial origin, with a cumulative glacial transport time of 6,361 ± 3,641 yrs (see section 3.3.2 for why). At maximum, particles are modelled to spend up to 12,644 and 14,613 yrs in ice for subglacial and supraglacial seeding, respectively (Fig. 6e, f). Particles yielding such high glacial transport times are few (<300) and frequency

686 distributions tail off, which indicates that starting our simulations at least 15 kyr before the local LGM (~24.8 ka) is both important and adequate (Fig. 6e, f). On average, ice-contact deposits of the Inn LGM

688 margins are modelled to have travelled over 78 ± 80 and 138 ± 81 km for sediments of subglacial and supraglacial origin, respectively. Ice-contact deposits of subglacial origin are estimated to have spent, on

690 average, a total of 353 ± 1936 yrs in ice-free conditions during their source-to-sink journey. This time in ice-free conditions occurs when particles are deposited following temporary ice retreat, prior to re-

692 entrainment by subsequent advances (see videos in supplement). This median number increases fivefold to 1885 ± 3719 yrs for sediments of supraglacial origin, suggesting a greater potential for atmospheric

694 exposure during their transport (assuming they remain at the Earth's surface). In line with these estimations, the results suggest that ice-contact deposits of the Inn LGM margins and of supraglacial origin

696 are on average eroded 5090 yrs earlier than those of subglacial origin (Fig. 6).

698 For these Inn glacier LGM margin deposits, the modelled trajectories of subglacially-seeded sediments display similar pathways than those of supraglacial origin. However, we find that glacial sediments of

700 supraglacial origin, due to reaching glacier surfaces from nunataks and valley/glacier sides, are more likely to produce trajectories resembling well-defined medial moraines (e.g. Fig. 6b, basins 170, 150). We find

702 this is rarely the case for modelled trajectories of subglacially-seeded particles, which can originate from across the glacier bed, including from valley/glacier centres where basal velocities are highest. This

704 difference also explains why subglacially seeded particles spread over the entire terminal perimeter of the Inn glacier's piedmont lobe during the LGM. However, particles of supraglacial origin rarely reach the

706 glacier's centreline and are pushed sideways by flow divergence within the piedmont lobe, causing preferential advection to both the left and right lateral margins of the terminal lobe, but not to its centre

708 (Fig. 6). We observe a similar trajectory differentiation between ice-contact deposits of subglacial versus supraglacial origin for the Garda (sink 17) and the Ticino-Toce (sink 48) outlet glaciers, towards their

710 modelled piedmont lobes (see 'sink-to-source' catalogue). This mechanism has important implications for sampling frontal moraines for detrital thermochronology and linking sampling locations to catchment

712 provenances (e.g. Bernard et al., 2020).

714 These results focus on a single LGM ice-contact deposit, or 'sink', as an example. The same data were obtained for all 49 mapped sinks (Fig. 3a) and can be viewed via the sink-to-source analysis catalogue
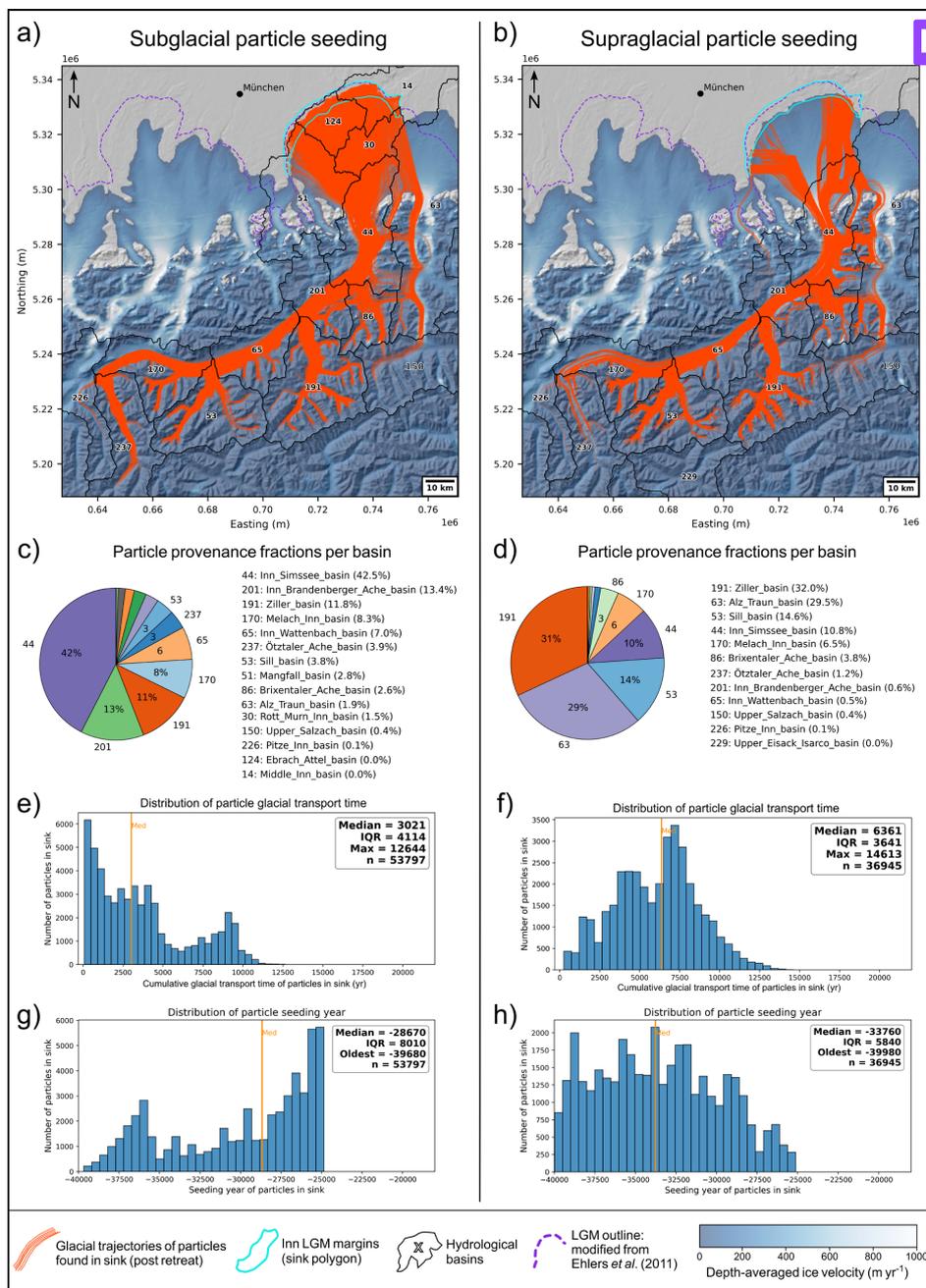
716 (link: https://doi.org/10.5281/zenodo.18374156).

718

720

722

Figure 6. Sink-to-source analysis and resulting modelled particle trajectories (a, b) and transport statistics (c-h) for subglacially (a, c, e, g) and supraglacially (b, d, f, h) seeded particles ending up in the chosen sink (cyan polygon) following final glacier retreat. Here, results are shown for a single example sink (or ice-contact deposit) from our sink-to-source catalogue (n=49 sinks in total), i.e. the Inn glacier LGM margins (sink 19: see Fig. 3a for location). The pie charts (c, d) and associated legends indicate the provenance fractions of all particles ending up in this sink for each hydrological basin (mapped and numbered in black on panels a, b) in which they were seeded (see Figure S1). Histograms (e-h) display the resulting distributions of sink particle cumulative glacial transport times and seeding years (i.e. particle age). 'IQR' stands for 'Interquartile Range': i.e. the spread of middle 50% of the dataset: 75th – 25th percentiles.

762

3.3.2 Ice-contact deposits of subglacial versus supraglacial origin

764

As described above for Inn glacier LGM deposits, we find notable differences in glacial transport histories

766 and characteristics between ice-contact deposits of subglacial versus supraglacial origin. Similar differences hold true when analysing all 49 sinks and the 3.1 million particles deposited within them (Fig.

768 7). For the majority of these sinks (41 out of 49), cumulative glacial transport time is on average greater for particles of supraglacial origin. When averaging over all sinks, the particle glacial transport time is

770 higher by approximately 1925 years, i.e. a factor of 1.9 increase. The total ice-free time (pre-deposition) of sink particles during their source-to-sink journey is also higher for those of supraglacial origin in 41 out

772 of 49 cases, and on average by 1519 yrs, a factor of ~2.74 increase (Fig. 7). We find a similar pattern for the age (i.e. the seeding year) of sink particles, which is older (on average by 4640 yrs) for those of

774 supraglacial origin in 46 out of 49 cases. Thus, our modelling suggests that in the Alps, LGM terminal ice-contact deposits of supraglacial origin were likely to be eroded earlier in time, spend more time in or on

776 glacier ice, and spend more time exposed in ice-free conditions during their full source-to-sink journey (Fig. 7). This is likely caused by glacial sediment of supraglacial origin reaching the glacier surface mainly

778 in accumulation areas, where steep topographies protrude, and where ice velocities are lower.

780 Unlike subglacially-eroded materials which are preferentially produced in fast-flowing areas often located closer to terminal deposits, supraglacial debris requires (on average) more time to be advected to lower

782 glacier elevations and areas of faster-flowing ice and, in turn, to the terminus. Moreover, glacial sediments of supraglacial origin tend to reach contact with ice towards slope-adjacent glacier sides, making them

784 likely to remain near lateral ice margins during glacial transport. This increases their chances of deposition during temporary periods of ice retreat and thinning, which can increase their cumulative ice-free time

786 during their source-to-sink journey. In contrast, subglacially-eroded sediments will preferentially be concentrated towards the faster-flowing centreline of glaciers, further away from lateral glacier margins.

788 These results have implications for terrestrial cosmogenic nuclide exposure dating of moraine sediments deposited by alpine glaciers and other topographically constrained icefields (Heyman et al., 2011). Indeed,

790 they imply that ice-contact deposits of supraglacial origin are more likely to yield cosmogenic nuclide inheritance signals relative to those of subglacial origin, not only because of pre-transport exposure, but

792 also due to potentially longer and more complex glacial transport histories. However, one must note that clast erosion during glacial transport can counterbalance this mechanism and instead remove nuclide

794 inheritance signals (Matthews et al., 2017) (more details in Discussion).
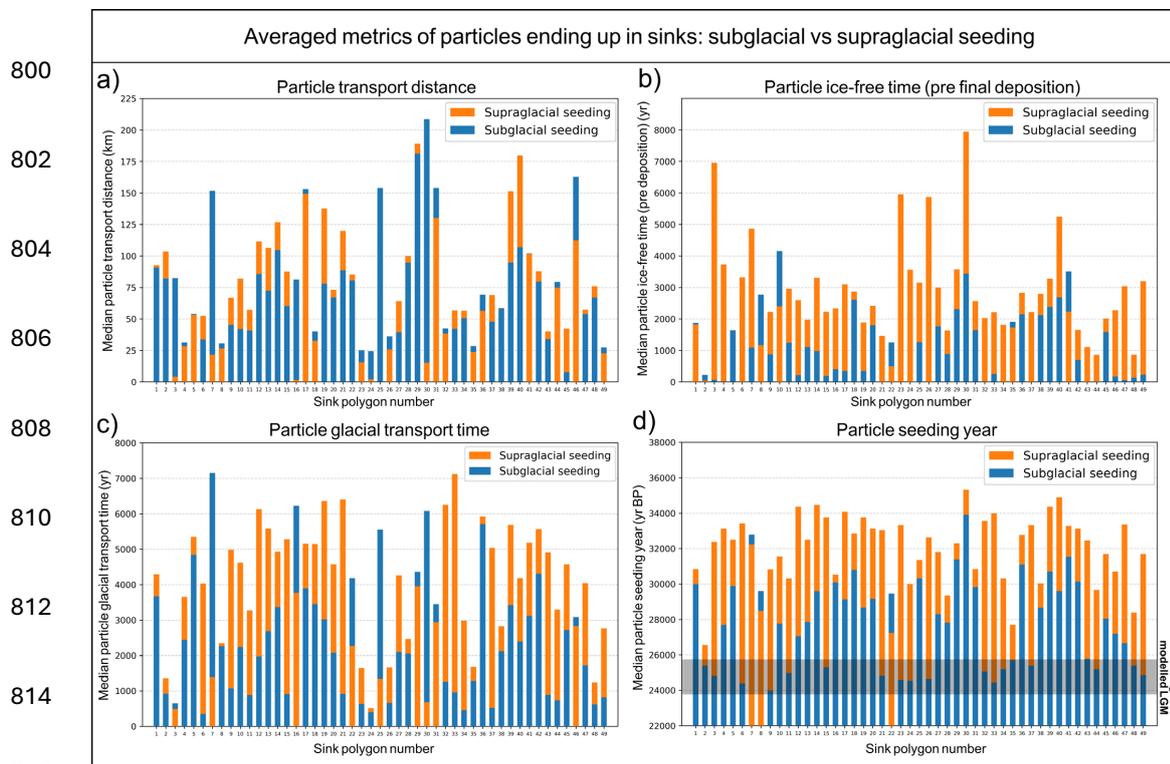
796

798

Figure 7. Overlapping bar plots (non-stacked) indicating particle statistics averaged over all sink particles (median) for each of the 49 sinks (or ice-contact deposits) in our catalogue (x axis), shown separately for both subglacial seeding (blue bars) and supraglacial seeding (orange bars). See Fig. 3a (or catalogue) to visualize the locations and names of these 49 sinks. The data are shown for four distinct particle metrics, i.e. the median sink particle transport distance (a), the median cumulative time a particle spent in ice-free conditions during its full source-to-sink journey (b), the median cumulative particle glacial transport time (c), and the median particle seeding year (i.e. the particle age) (d). For all metrics except transport distance, modelled sink particles of supraglacial origin tend to display higher median values (orange bars taller than blue bars), suggesting that, on average, they tend to be older (i.e. seeded earlier), spend more time in glacier ice, and spend more time in ice-free conditions during their source-to-sink journey, relative to sink particles of subglacial origin.

3.3.3 Addressing 'sink-to-source' debates: The Mont Salève erratics case study

To demonstrate that our modelled glacial sediment trajectories can help address tangible research questions and scientific debates in the Alps, we conduct a specific analysis for the example of the Mont Salève erratics. The Mont Salève, located 10 km to the south of Geneva, is a ~600 m tall, ~16 km long, and ~2.5 km wide limestone mountain part of the Jura Massif. The Salève features a flat plateau-like summit (~1300 m a.s.l.) displaying approximately 400 preserved erratic boulders (1200 pre-exploitation) officially protected since 1877 and subject to investigations since (e.g. Coutterand, 2010). Some of the erratics were geologically identified as Gneiss from the Siviez-Michabel nappe (Valais, Switzerland) while

others as Mont-Blanc granite. They were hypothesised to have been deposited during retreat phases and

840 thinning from the largest Late-Pleistocene glaciations of the AIF. More specifically, Coutterand (2010) attributed their glacial transport and deposition to two separate glacier systems; i) the Rhône glacier

842 flowing along the Rhône valley and Geneva Lake basin thus reaching the Salève from the northeast, and ii) the Arve glacier flowing along the Arve valley and originating from the Mont-Blanc Massif thus

844 reaching the Salève from the southeast. Our study enables to compare these hypotheses against modelled estimates for the first time. Firstly, our results suggest the Mont Salève summit was covered by a thin (~30

846 - 100 m) layer of ice during the LGM, when peak AIF extent and volume was reached (~24.8 ka; Leger et al., 2025) (Fig. 8). When tracking the trajectories of all particles deposited on the Mont Salève following

848 deglaciation, we find that no particles are modelled to be deposited by the Arve glacier (Fig. 8). Instead, between 40 and 18 ka, 100% of modelled ice-contact deposits on the Salève are deposited by the Rhône

850 glacier, with glacial sediment travelling exclusively along the western side of the Rhône valley and the southern side of the Geneva Lake basin (Fig. 8). The seeding locations of particles deposited on the Salève

852 trace back to the northeastern sectors of the Mont-Blanc Massif, thus overlapping Mont-Blanc granite outcrops, but also to the Dranse de Bagnes, Dixence, and Val-d'Hérens valleys (Vallais, Switzerland) thus

854 overlapping the Siviez-Michabel gneiss nappe (Bigi et al., 1990) (Fig. 8). Thus, in our simulations, the geographical origin of both subglacially- and supraglacially seeded particles can explain the lithologies of

856 erratic boulders found on the Salève plateau (Fig. 8).

858 The lack of Salève-deposit trajectories associated with the Arve glacier is related to the modelled dynamics of confluence between the Rhône and Arve glaciers. Our simulations suggest that during the last AIF

860 advance preceding the LGM (~28-26 ka), a branch of the more voluminous and thicker Rhône glacier expanded southward from the Geneva Lake basin into the Arve valley and around the southeastern flanks

862 of the Salève. This modelled expansion generates enough driving stress to push the thinner Arve glacier, forced to redirect its flow south-westward due to its lower ice discharge rate (Fig. 8). Consequently, our

864 simulations suggest the Mont Salève remained surrounded by ice exclusively from the Rhône glacier during the LGM and until final deglaciation from the area (~20 ka in our simulations). More empirical

866 investigations and dating of the Salève erratics are needed to either validate or discard this new model-derived hypothesis, which differs from the previous empirical hypothesis (Coutterand, 2010). Regardless,

868 this study case of the Mont Salève erratics is a prime example demonstrating how Alps-wide modelling of glacial sediment transport can help address questions on past glacier flow dynamics and the former

870 transport history of certain ice-contact deposits.

872

874
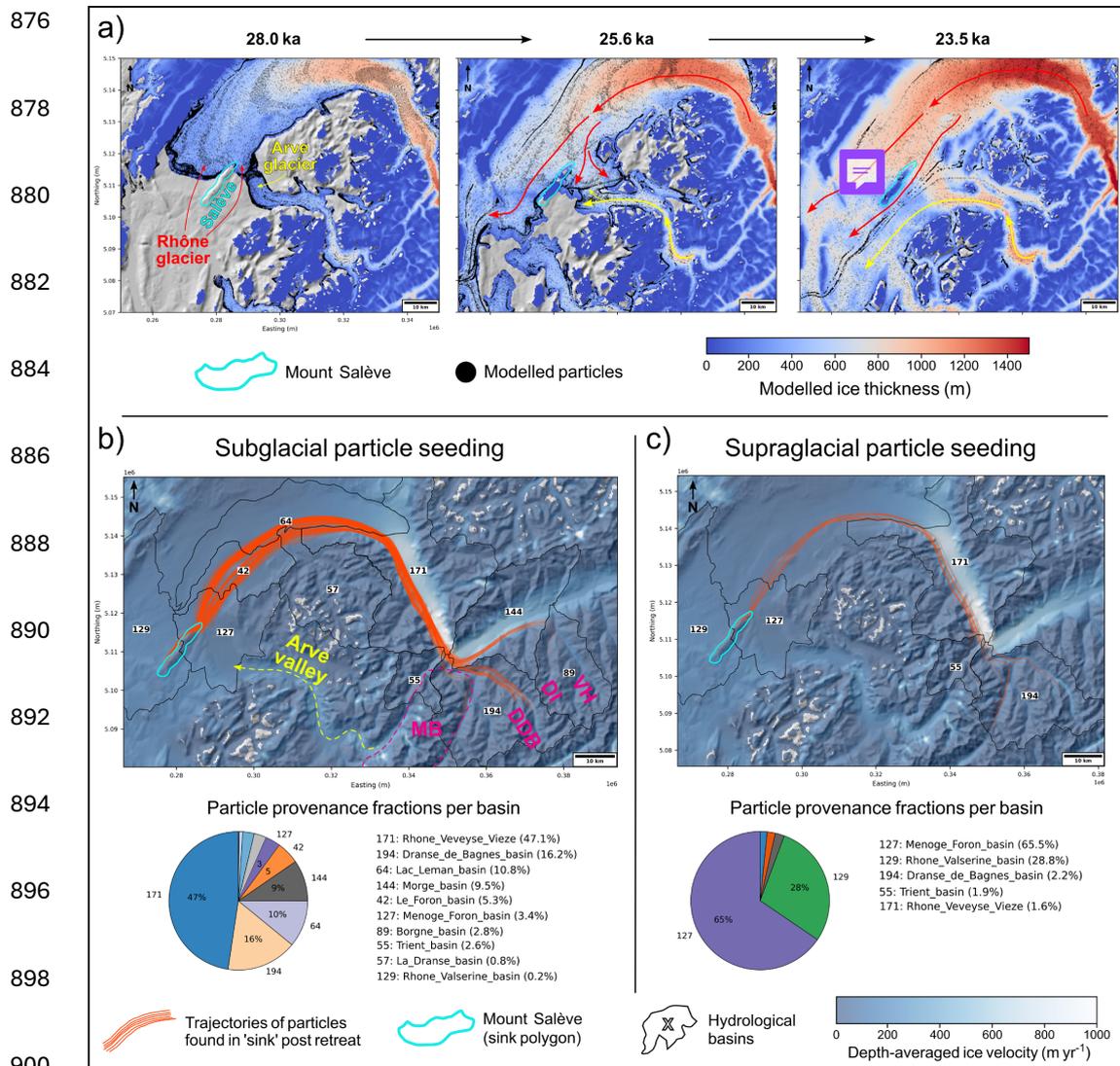
Figure 8. Instructed Glacier Model (IGM) output, sink particle trajectory maps, and sink particle provenance fractions per hydrological basin, for the Mont Salève erratics case study (see section 3.3.3). The three ice-thickness model output snapshots (a) at 28, 25.6, and 23.5 ka display the modelled ice thickness fields in the region of the Mont Salève indicating how the Rhône and Arve glaciers interact in our model. More specifically, they show how, in our simulation, the Rhône glacier pushes the ice from the Arve glacier towards the southwest forcing it to redirect its flow: causing the Mont Salève to be surrounded by modelled ice exclusively from the Rhône glacier during the entire Last Glacial Maximum (LGM). This in turn explains the resulting particle glacial-transport trajectories (b, c), highlighted by orange lines, shown for particles ending up on and around the Mont Salève following final ice retreat. These suggest no ice-contact deposits of the Mont Salève are modelled to be transported by the Arve glacier. They are instead all exclusively transported by the Rhône glacier. Note particle seeded within Basin 129 (28% of particles for supraglacial seeding) are only local to Mont Salève: i.e. particles from near the summit moved downslope and which still end up within the mapped polygon following final ice retreat. On panel b; 'MB', 'DDB', 'DI', and 'VH' stand for the 'Mont-Blanc Massif', and the 'Dranse de Bagnes', 'Dixence', and 'Val-d'Hérens' valleys, respectively, enabling to locate places mentioned in main text (section 3.3.3).

918

3.4 The source-to-sink analysis and catalogue

920

With the source-to-sink analysis, we produce a second catalogue of time-transient (40-18 ka) glacial

922   sediment trajectories for a selection of key surface lithologies across the Alps, hereafter referred to as our

'sources' (see section 2.4) (link: https://doi.org/10.5281/zenodo.18374156). These trajectories reveal the

924   pathways of particles seeded either subglacially or supraglacially within source polygons (n = 22; Fig.

3b). For each source polygon and seeding type, we provide a high-resolution map of source particle

926   trajectories. We interpret these source-to-sink trajectories as model estimates of possible locations (along

the modelled trajectories) where sediments of a specific surface lithology may have been transported to

928   and deposited by ice between 40 and 18 ka. These locations can then be compared against the coordinates

of documented deposits (e.g. erratic boulders) of known lithology, which may help assess the accuracy of

930   our modelling.

932   *3.4.1 A source-to-sink case study: the 'Arolla Gneiss' trajectories*

934   As an example from our catalogue, we here describe our source-to-sink analysis for a single lithology, i.e.

Arolla Gneiss (source number 4 in the catalogue: Fig. 9). This lithology is part of the Austroalpine system

936   of the western Alps and, more specifically, of the Dent Blanche and Sesia Lanzo composite nappe-system

of Paleoafrican provenance (Manzotti, 2011). It was formed during the Early-Alpine and Lepontine

938   tectonometamorphic events and is mainly composed of greenschist orthogneisses from Late-Hercynian

granitoids (Bigi et al., 1990a). This lithology outcrops mainly within the Dent Blanche, Dent d'Hérens

940   and Weisshorn Massifs (Swiss Alps), and along a narrow band of the southern Italian Alps stretching for

~160 km from the Valle di Viù to the Melezza valley and Locarno (Ticino, Switzerland) (Fig. 9). Numerous

942   erratics deposited in the Swiss and Italian alpine forelands are of Arolla-Gneiss lithology (e.g. Graf et al.,

2015).

944

In our simulations, Arolla Gneiss is modelled to be eroded and transported by ice into vastly different

946   valleys and outlet glacier catchments following diverse and complex trajectories (Fig. 9). It is for instance

modelled to be transported by the Rhône outlet glacier reaching the Lyon outlet glacier (France), but also

948   by the Solothurn outlet glacier (Switzerland), the Dora Baltea outlet glacier reaching the Ivrea morainic

arc (Italy), and the Ticino-Toce outlet glacier (Italy) (Fig. 9). Arolla Gneiss trajectories enable us to

950   visualize how modelled ice flux from the upper Rhône glacier diverges over the northern Lake Geneva

flanks during the LGM, as previously modelled (e.g. Jouvet et al., 2017). Indeed, it reveal how modelled

952   ice flowing along the true right side of the Rhône valley (between Martigny and Montreux, Switzerland)

bends eastwards and heads towards Solothurn, while ice flowing along the true left side of the Rhône

954   valley bends south-westwards along the Geneva Lake and heads towards the Lyon outlet glacier (Fig. 9).

956   Interestingly, some of the particles heading towards Solothurn are pushed against the southeastern Jura
       flanks in locations of modelled ice transfluences causing glacial transport through the Jura mountains, into
958   the Doubs valley and towards the northern margins of the Jura icecap (France) (Fig. 9). Our simulations
       thus produce transfluences of alpine ice overflowing the Jura mountains during peak LGM extent and
960   volume (~24.8 kyr). These transfluences are modelled in three broad locations, firstly towards the Vallorbe
       pass and the valley of the Jougnena (46°43'N; 6°23'E), secondly towards Baulmes and Sainte-Croix (East
962   of the Mount Suchet: 46°48'N; 6°30'E), and thirdly directly West of Vallorbe over the 'Grotte aux Fées'
       cave and the Combe du Puits area (46°42'N; 6°19'E). Former expansions of alpine glaciers overflowing
964   the Jura mountains are thought to have occurred during pre-LGM maximum Late-Quaternary glaciations
       such as during Marine Isotope Stage (MIS) 12, 10, 8, or 6 (Keller and Krayss, 2011; Preusser et al., 2011;
966   Graf et al., 2015). However, no published evidence yet exists for such transfluences during the LGM (MIS
       2) (Campy, 1992; Buoncristiani & Campy, 2011). Our model may either slightly overestimate ice thickness
968   over the Rhône and Solothurn glaciers during the LGM, or may be correct but sedimentological evidence
       for such momentary transfluence may be rare and not yet documented/dated. The modelled Arolla-Gneiss
970   trajectories reveal other surprising and complex pathways, such as possible transport of glacial sediments
       up into the Aulps valley (Morzine river valley, France) by ice from the Rhône glacier which, in our model,
972   generates southward ice-flow upvalley from the Geneva Lake basin (Fig. 9). Key differences can be
       observed between modelled Arolla-Gneiss trajectories of particles seeded subglacially versus
974   supraglacially. Within the Rhône glacier catchment, Arolla-Gneiss outcrops are confined to high-elevation
       topographies located towards the glacier's upper accumulation zone, where nunatak occurrence and
976   rockfall potential are high, and where modelled basal ice velocities remain relatively low (<50 m yr^{-1}).
       Thus, within the Rhône glacier catchment, supraglacially seeded particles from Arolla-Gneiss outcrops
978   yield a higher number and diversity of modelled trajectories, relative to subglacially-seeded particles (Fig.
       9). In the southern Italian Alps, particle trajectories show the opposite, with numerous outcrops located in
980   fast-flowing ice regions leading to higher numbers of trajectories and ice-contact deposit locations for
       particles of subglacial origin.

982

984

986

988
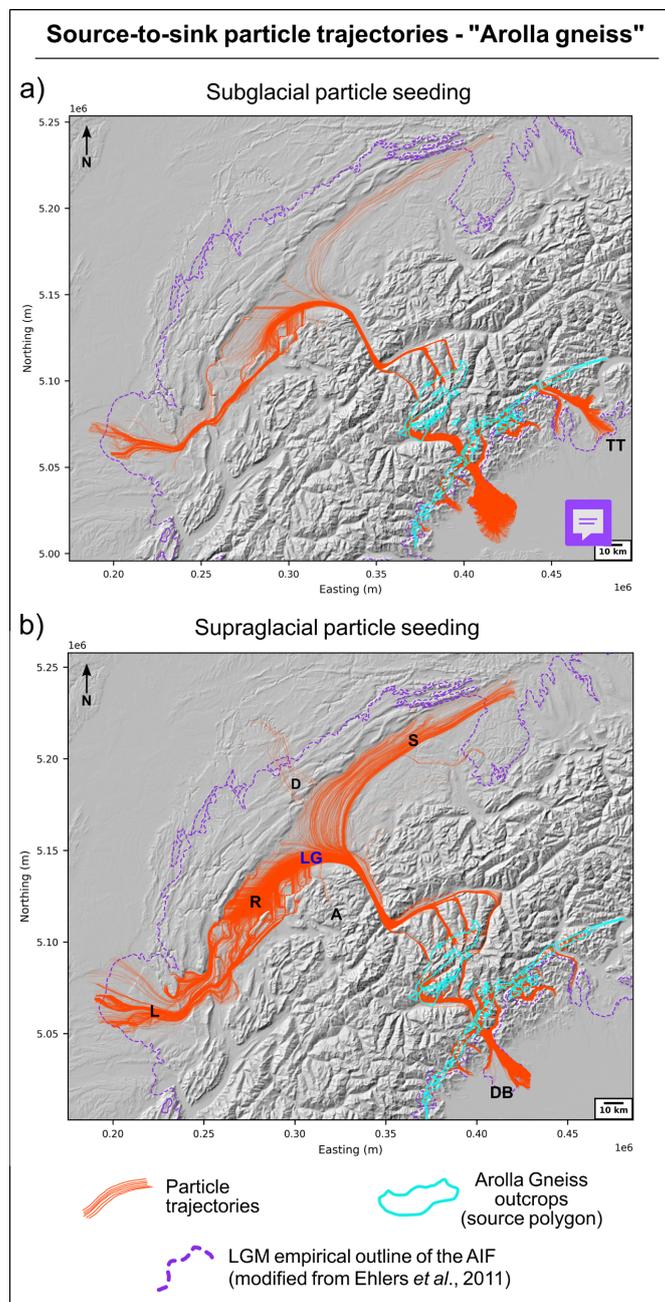
990

Figure 9. Source-to-sink analysis and resulting particle glacial-transport trajectories for all particles seeded within an example source polygon; in this case a single surface lithology from our source-to-sink catalogue (n=22 surface lithologies), i.e. the Arolla Gneiss (originally mapped by Bigi et al., 1990). Particle trajectories are shown for both subglacial (a) and supraglacial (b) seeding. We interpret these source-to-sink trajectories as model estimates of possible locations (along the entire trajectories) where ice-contact deposits of the Arolla-gneiss lithology may have been transported to and deposited by glaciers between 40 and 18 ka (time frames of simulations). The labels 'A', 'DB', 'D', 'L', 'LG', 'R', 'S', 'TT' stand for: 'Aulps valley', 'Dora-Baltea outlet glacier', 'Doubs valley', 'Lyon outlet glacier', 'Lake Geneva', 'Rhône glacier', 'Solothurn outlet glacier', 'Ticino-Toce outlet glacier', respectively, and relate to places/features mentioned in the main text (section 3.4.1).

3.4.2 Model-data comparison with dated erratics

Our 'source-to-sink' analysis provides the opportunity to test model agreement against data from ice-contact deposits of known provenance. Here, we conduct such a model-data comparison by compiling peer-reviewed publications which dated erratic boulders in the Alps to the time range of our simulations (40-18 ka) using terrestrial cosmogenic nuclide exposure dating (Table S1). The compiled erratics need to feature a lithological description that is specific enough (e.g. 'Central Aar granite') to be associated to a well-defined and spatially restricted lithology (unlike 'limestone', for instance). Moreover, only one sample per location (i.e. a sampling site in original studies) is considered for this test, to reduce statistical biases. A total of 38 erratic boulders were found to match these requirements, published in 13 separate studies (Ivy-Ochs et al., 2004; Gianotti et al., 2008; Reber et al., 2014; Graf et al., 2015; Bichler et al., 2016; Wüthrich et al., 2018; Ivy-Ochs et al., 2018; Boxleitner et al., 2019; Prud'homme et al., 2020; Braakhekke et al., 2020; Kamleitner et al., 2022; Kamleitner et al., 2023; Roattino et al., 2023). Exposure ages were re-calculated consistently as part of the AlpIce geochronological database (Kamleitner et al., *in prep*). Modelled particle trajectories (subglacial and supraglacial seeding combined) for the relevant source lithology successfully overlap the locations of erratic boulders of that lithology in 26 out of 38 cases (Table S1). The trajectories thus fit empirical data in 68% of cases. This number would moreover increase to 81% would we tolerate a small (<4 km) increase in ice extent in locations where our model slightly underestimates ice extent during the LGM, relative to mapped terminal moraines (see Fig. 1a, 4a in Leger et al., 2025). Thus, clear model-data misfit is only observed in 18% of cases (10 boulder samples). These results suggest our LGM model of the AIF coupled with our particle-seeding and 3D tracking schemes can transport particles to appropriate locations, for the majority of the compiled erratics (Table S1).

3.5 Detecting LGM ice transfluences across the Alps

As shown above with the example of Arolla Gneiss 'source-to-sink' trajectories overflowing the Jura Massif, the coupling of 3D particle tracking enables us to estimate, for the first time, the precise locations and time span of ice transfluences in the Alps during the LGM (Fig. 10). Ice transfluences occur when the growth of ice sheets and/or icefields cause the formation of topographically uncoupled ice domes, i.e. which accumulate away from summits and hydrological catchment divides. If the surface elevation of these domes exceeds the altitude of neighbouring cols, uncoupling from main hydrological catchments occurs causing ice-flow to cross main hydrological divides (Linton, 1949). This can result in glacial sediment transport over high-elevations ridges/cols and into different catchments (Monegato et al., 2022) (Fig. 10). Reconstructing LGM transfluences can thus help understand former ice-flow dynamics and unravel the puzzling lithologies/provenances of certain ice-contact deposits in the Alps (e.g. Reitner et al.,

2010). Here, we loaded our modelled particle trajectories and thus 3D ice-flow lines into a geographic

1070 information software (ArcGIS Pro 3.4) to detect the occurrence of ice transfluences in our simulations, focusing only on the 11 largest hydrological catchments of the Alps (Rhône, Aare, Rhein, Isar, Inn, Enns,

1072 Drau, Piave, Brenta, Adige, Po) (Lehner & Grill, 2013). We present this analysis' results in a series of maps (Figures S8-14) highlighting the locations of modelled ice domes, flowlines, and ice transfluences

1074 across the Alps. Figure 10 shows one of these maps for the example region of the upper Inn catchment. There, the build-up of the 'Engadin' ice dome centred towards Zernez (46°41'N, 10°05' E, 1465 m a.s.l.)

1076 and reaching a modelled maximum ice surface elevation of ~3100 m a.s.l. leads to a complex network of topographically uncoupled flowlines causing a high concentration of ~30 ice transfluences into the

1078 adjacent Rhein, Adda, Adige, and Isar catchments (Fig. 10). This causes, for instance, modelled ice from the Inn valley between St.-Moritz (46°29'N; 9°50'E) and Zernez (a 45 km stretch) flowing south-

1080 westwards over the Maloja pass (46°24'N; 9°41'E) into the Val Bregaglia, Como Lake basin, and feeding the Adda and Seveso outlet glaciers (sinks 2 and 44 in 'sink-to-source' catalogue). As another example,

1082 we note that our model reproduces the well-documented Simplon pass transfluence (e.g. Florineth & Schlüchter, 1998; Kelly et al., 2004; Dielforder & Hetzel, 2014), with ice possibly transporting sediments

1084 from the Eiger-Mönch-Jungfrau mountains (e.g. Aar granites) across the Rhône valley, over the Simplon pass, and into the Ticino-Toce glacier system during the LGM (sink 48 in 'sink-to-source' catalogue,

1086 Figure S11). In our simulations, we also find that modelled ice is nearly always warm-based towards the main ice domes and transfluences occurring during the LGM (see Fig. 6b in Leger et al., 2025). Moreover,

1088 the modelled time span of transfluence occurrence is highly case-specific and can vary from 1-3 kyr, thus only during peak LGM conditions, to up to nearly the full simulation time frame (i.e. 22 kyr) and LGM

1090 period (e.g. the Engadin ice dome, Fig. 10). Consequently, our results show that coupling 3D Lagrangian particle tracking to glacier evolution modelling can also help identify the detailed events of complex and

1092 momentary topographic uncoupling of ice-flow during major Quaternary glaciations of the Alps.

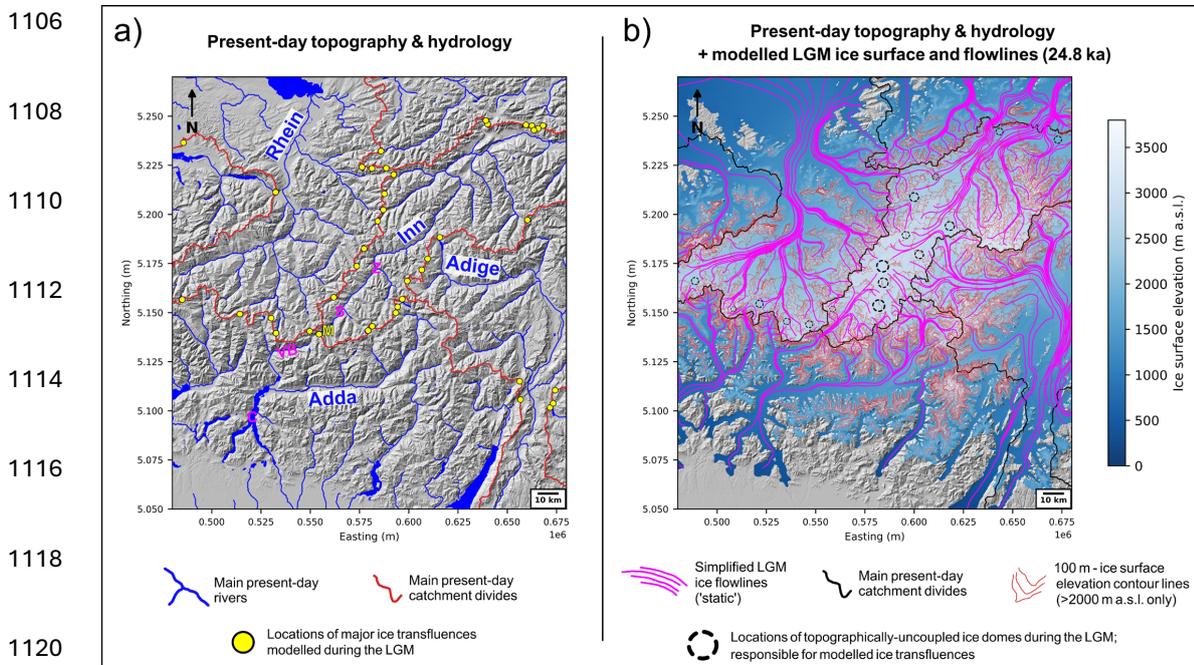1094

1096

1098

1100

1102

1104

Figure 10. Map of modelled ice surface elevations and simplified 'static' ice flowlines (pink lines) during the LGM (~24.8 ka) in the region of the Engadin ice dome, with locations of modelled ice transfluences (yellow dots on panel a). These transfluences can explain the complex provenance of certain ice-contact deposits. We quantified them for the 11 largest river catchments of the Alps, whose divides are shown in red on panel a, and black on panel b. A series of six figures displaying the same ice-transfluence analysis for five other regions of the Alpine Ice Field (AIF) are available in the Supplementary Materials. Note that whilst useful for the visual purpose of this figure, the simplified glacier flowlines (pink lines) shown here (panel b) are drawn from so-called 'static' flowlines, which are non-time-transient and only obtained from the depth-averaged ice velocity field modelled during a single time frame: i.e. the maximum AIF volume; at 24.8 ka. These should only be considered useful to visualize the modelled flow direction of ice at the precise locations of transfluences and only during peak LGM. The substantially more complex and accurate time-transient flow trajectories obtained from our 3D Lagrangian particle tracking, displayed in Figures 6 and 9 for example, are more diverse and representative of the modelled time-transient ice-flow trajectories, but would make visualizing transfluences on this figure impossible given the large number of modelled particles and resulting cross-cutting trajectories (see Figure S7). On panel a, the 'C', 'M', 'S', 'VB', and 'Z' labels stand for 'Lake Como', 'Maloja pass', 'St. Moritz', 'Val Breglaglia', and 'Zernez', respectively, and relate to locations mentioned in main text (section 3.5).

3.6 Particle trajectory sensitivity to model parameters

To assess the sensitivity of our particle trajectories to both the seeding scheme and model parameters, we conduct two additional AIF simulations that differ from the original setup presented above like so: i) The first sensitivity test uses a 'simple' seeding scheme, which is not process-based and instead creates particles supraglacially in a spatially- and temporally-regular manner, i.e. with seeding occurring in 20% of grid cells exclusive to the accumulation zone, and regularly every 300 yrs. ii) The second sensitivity

1148   test uses the same 'complex' seeding as the original scheme (Fig. 2) but employs the parameter values of
a different ensemble simulation (i.e. number 24) within the set of 8 Not-Ruled-Out-Yet simulations

1150   obtained by Leger et al. (2025). Whilst featuring different ensemble-varying parameter values (see Table
S1 in Leger et al., 2025), simulation 24 produces Alps-wide model-data agreements in LGM ice extent

1152   and thickness that are indistinguishable from simulation 37 (used throughout this study). Input parameter
differences (n=10) however generate changes in SMB, the basal sliding parameterization, ice rheology,

1154   and the magnitude of isostatic deflection. Importantly, simulation 24 uses a different bed topography than
simulation 37, with no removal of valley-fill sediments.

1156

   In the first sensitivity test, which uses 'simple' seeding instead, model agreement with the locations of

1158   dated erratics presented above (section 3.4.2), using our source-to-sink analysis, decreases from 81-68%
to 74-58%. These two ranges represent whether we tolerate the small (<4 km) increase in ice extent

1160   mentioned above (section 3.4.2). Whilst not substantial, this decrease in model-data agreement is
noticeable and suggests that a less process-based particle seeding scheme leads to a worse model-data fit

1162   on the provenance, glacial transport, and deposition histories of ice-contact deposits during the LGM. In
the second sensitivity test, as the seeding scheme is unchanged from the original (see section 2.2), we can

1164   use provenance fractions (%) per hydrological basin (n=241) for each sink (see section 2.4) to quantify
inter-simulation differences. Here, when using parameters from Leger et al. (2025)'s ensemble simulation

1166   24 instead of 37, we find that particle provenance fractions per hydrological basin (e.g. percentages in
Figs. 6, 8) remain identical in ~72% of cases, on average (median difference: 28.5%). When comparing

1168   particles' provenance basins irrespective of fraction percentages, we find sink particles originate from the
same basins in 88.5% of cases. Thus, running a simulation which yields a similar LGM model-data fit but

1170   uses different sensitive parameter values causes sink particles to originate from different basins in 11.5%
of cases and provenance fractions to vary by 28.5% on average. These results show a non-negligible inter-

1172   simulation variability highlighting a noticeable sensitivity of particle trajectories and provenances to
modelled ice dynamics and/or bed topography changes. However, this test also shows that the majority of

1174   particle trajectories, provenances, and glacial transport histories remain unchanged relative to the original
simulation.

1176

1178   **4 Discussion**

1180   **4.1 Limitations and future work**

1182   The computational gains of GPU-based glacier modelling coupled with 3D Lagrangian particle tracking
enabled us to produce, for the first time, an Alps-wide estimation of transient glacial sediment pathways

1184   during the last glaciation (40-18 ka). Although our model-data comparison of source-to-sink trajectories

31

1186   yields promising results with between 81% and 68% model fit with dated erratics' locations (section 3.4.2, Table S1), this study should be considered a first-order attempt yielding limitations and room for improvement. We here describe the main limitations of the assumptions made in this experiment,

1188   providing suggestions for improvement in future modelling work of similar nature.

1190   In this study, we assume passive particle glacial transport with no interaction with ice rheology and flow dynamics. In reality, supraglacial debris can influence glacier surface mass balance through insulation

1192   (e.g. Rowan et al., 2015) while basal ice sediments can alter basal friction and thus glacier sliding velocities (Hallet, 1981; Iverson et al., 2003). Our modelling also assumes all glacial sediment to move at

1194   the same velocity as the ice. Whilst this is a common modelling assumption (e.g. Rowan et al., 2015; Jouvet et al., 2017; Bernard et al., 2020; Margirier et al., 2025), the drag force in Stokes Law can cause

1196   resistance and lower velocities for clasts advected within highly viscous fluids (e.g. ice; Byers et al., 2012). Moreover, complex mechanisms of sediment storage occur (e.g. lodgement tills) at partially coupled ice-

1198   bed interfaces causing sediment advection speeds below ice velocity (Alley et al., 1997; Evans et al., 2006). On the contrary, gravitational and fluvio-glacial transport within glacier systems can generate

1200   sediment advection speeds greater than ice velocity (Walder and Fowler, 1994). Gravitational englacial transport also occurs when a glacier features numerous fractures in which debris can fall, a mechanism

1202   that is not yet modelled in glacier-wide simulations. Sediment transport by rivers (proglacial) and subglacial drainage, whilst not modelled in this study, can also complexify deposits' transport histories by

1204   moving large sediment volumes further down-river prior to glacier re-entrainment (Lane et al., 2017). In future work, modelling these complex mechanisms would require full coupling of both subglacial

1206   hydrology and sediment-transport modules to glacier-evolution models (Delaney et al., 2023).

1208   We assume all sediment to be fully preserved during glacial transport, and that variability in ice-contact deposit provenance is exclusively controlled by variations in seeding and glacial transport histories.

1210   However, clast erosion during glacial transport also plays an important role. Indeed, glacial sediments transported over greater distances are more likely to spend time at the ice-bed interface where they

1212   typically undergo abrasion, crushing, or truncation (Boulton, 1978). With increasing time and transport distance, this can generate rounding and comminution of coarse sediments (e.g. boulders, cobbles) into

1214   finer fractions (e.g. silts, sands and gravels) which can be mobilized by subglacial hydrology and evacuated downstream. Subsequently, the likelihood of finding sediments from a specific source in ice-

1216   contact deposits tends to decrease with increasing distance from that source (Humlum, 1985). In future modelling work, more realistic provenance fractions may thus be obtained through parameterizations that

1218   reduce particle preservation as glacial transport time and distances increase.

1220   Our particle seeding scheme assumes that all bed surfaces are equally susceptible to subglacial erosion and production of supraglacial debris via gravitational mass wasting. This is a simplification as different

1222   lithologies yield different hardnesses and varying susceptibilities to abrasion, plucking, frost shattering, weathering, and other erosion mechanisms (Moosdorf et al., 2018). The subglacial erosion susceptibility

1224   of distinct outcrops is also often dependent on local tectonic pre-conditioning (e.g. degree of rock faulting and fracturing). The accuracy of future coupled glacier-particle modelling may thus be increased by adding

1226   an erodibility index parameter controlling the seeding likelihood based on rock hardness, faulting, temperature-driven rock-permafrost conditions, and resistance to erosion, constrained by present-day

1228   geological observations and/or reconstructed past erosion rates (Gallach et al., 2021).

1230   Soft beds under temperate glaciers can become saturated with meltwater, leading to reduced effective pressure, lower basal yield stress, and faster sliding velocities (Iverson et al., 1995). While a meltwater

1232   feedback on sliding is included in our thermo-mechanically coupled glacier model setup (Leger et al., 2025), we consistently assume a positive correlation between sliding velocities and subglacial particle

1234   seeding through abrasion and plucking (Fig. 2). However, this may not always be the case as water saturation of soft beds and reduced effective pressure can instead shield bed material from

1236   abrasion/plucking reducing sediment mobilization or causing local soft bed deformation to instead dominate (Boulton, 1979).

1238

1240   Finally, while our GPU-based approach enables us to track an unprecedented number of particles in ice (~20.5 million) given our simulations' spatio-temporal scales, sediments are ubiquitous in real glaciers. Therefore, our modelling, which also does not include the re-mobilization by glaciers of pre-LGM

1242   sediment deposits, likely still underestimates the diversity of pathways glacial sediments may follow within a glacier system as complex as the former AIF during Late-Quaternary glaciations. However, as

1244   shown with this work, GPU-computing enables coupled glacier-particle modelling to become orders-of-magnitude cheaper and more computationally efficient. This should motivate new modelling studies of

1246   this nature to include the tracking of large particle numbers, thus helping to identify the particle numbers that more fully represent the ubiquitous nature of glacial sediments within icefield and ice-sheet systems.

1248

1250   Given the limitations summarized above, it is clear our modelling does not fully capture the complexity of glacial sediment sourcing and transport on multi-millennial, Alps-wide scales. Therefore, the diversity of 1) provenances and glacial transport pathways for a given ice-contact deposit, and 2) possible ice-

1252   contact deposit locations for a given source lithology, are likely underestimated by our 'sink-to-source' and 'source-to-sink' analyses (e.g. Figs. 6, 9). However, we believe that our simulations still capture the

1254   majority of former glacial sediment transport pathways, as evidenced by the relatively good model-data fit obtained (81-68%) when comparing modelled particle trajectories for a given lithology with data on

1256   LGM-dated erratic locations (section 3.4.2, Table S1).

1258   As described above (section 2.4), our sink-to-source analysis uses a subjective set of 49 sink polygons (Fig. 3a) covering the space between maximum time-independent margins of the modelled AIF and the

1260   updated LGM empirical outline of Ehlers et al. (2011). Our sink polygons thus result from a consistent yet highly simplified Alps-wide separation of large regions containing the LGM margins of former AIF outlet

1262   glaciers. An obvious future improvement would be to produce a similar sink-to-source analysis for a more detailed map of individual glacio-terminal landforms and ice-contact deposits that remain preserved to

1264   this day, thus enabling a more accurate model-data comparison. However, this would require producing a digital (e.g. GIS database), open-access, Alps-wide map of preserved glacial geomorphology with

1266   geochronological constraints and a consistent naming convention (e.g. Glasser & Jansson, 2008; Clark et al., 2018). To our knowledge, such a valuable product is not yet available for the European Alps.

1268

4.2 Coupled glacier-particle modelling; wider implications and perspectives

1270

4.2.1 New perspectives for paleo glacier model-data comparisons

1272

After modelling the final retreat of the AIF from its LGM margins (24-18 ka), our particle advection

1274   scheme deposits static particles in deglaciated regions which form moraine-like shapes (e.g. Fig. 11, Figures S3-6). The resulting spatial densities and shapes of these particle deposits are controlled by; 1) the

1276   modelled ice-margin shape and location at a given time, 2) the modelled ice margin retreat rate and residence time during maximum glacier extent, still-stands, and/or smaller re-advances, and 3) the supply

1278   of ice-advected particles to the glacier margins at a given model location and time. To improve the accuracy of the model regarding these three mechanisms, one could compare the spatial patterns of

1280   modelled particle deposits against the preserved glacio-geomorphological record (Fig. 11, Figures S3-6). Although this is not within the scope of this study, we believe this work opens the possibility to design

1282   new post-processing tools to automatically quantify the agreement between modelled particle deposits (post deglaciation) and preserved landforms such as terminal and lateral moraines. This could represent a

1284   novel approach to paleo model-data comparison that may complement existing tools (e.g. Ely et al., 2019; Archer et al., 2023, Veness et al., 2025) designed to automatically score transient paleo simulations and

1286   quantitatively evaluate model sensitivities to - and the adequacy of - input parameterizations and climate forcings (Fig. 11). Such comparison may also help identify mechanisms controlling the spatial

1288   heterogeneity of preserved ice-contact deposits found across deglaciated forelands and valleys today (Ivy-Ochs et al., 2022).

1290

1292

1294
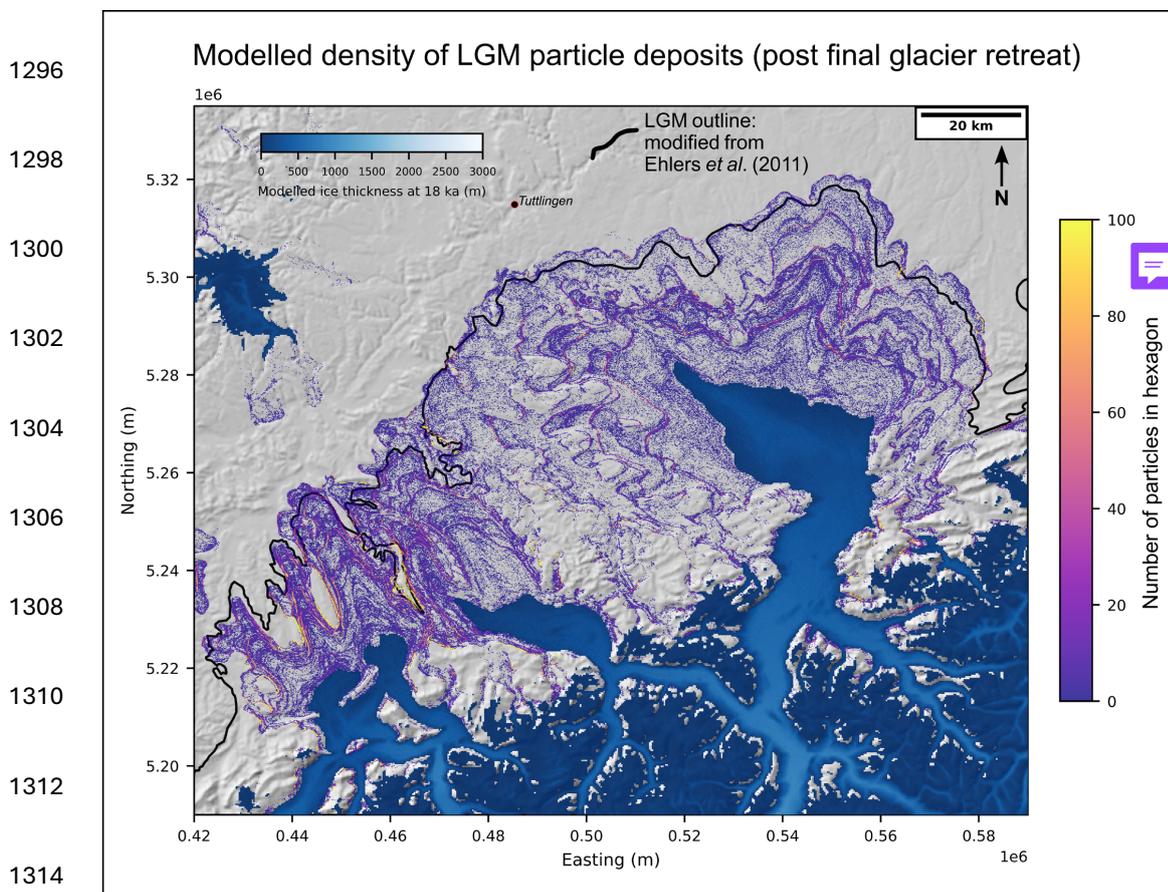
Figure 11. Map of modelled particle deposit densities located in modelled ice-free regions at 18 ka, the final timestep of our Alpine Ice Field (AIF) simulations of the Last Glacial Maximum (here 40-18 ka), and for the foreland region of the Rhein, Linth, and Reuss outlet glaciers. The AIF model output is displayed using modelled ice thickness at 18 ka. The particle deposit data shown here combines both datasets of particles seeded subglacially and supraglacially and is expressed as a spatial density map. Each colored dot is a small hexagon in which the total number of deposited particles is computed. Bright yellow colors indicate hexagons holding the highest concentrations of deposited particles. This model output clearly highlights periods of outlet glacier advances and/or margin stabilization during our AIF simulations through formation of moraine-shaped particle deposits. We argue the novel ability to produce such results over large spatio-temporal scales with our GPU-based Lagrangian particle tracking coupled to glacier evolution modelling may provide room for future model-data comparison exercises that quantify the fit between modelled particle deposits and the preserved glacio-geomorphological record (see Discussion section).

4.2.2 A method to investigate complex internal ice-flow dynamics

Lagrangian particle tracking coupled with glacier modelling essentially offers a mechanism to better visualize the time-transient 3D flow trajectories of simulated glacier motion (Figure S7). As a result, it can help to better understand contemporary and past internal glacier dynamics, including vertical ice motion,

flow convergence and divergence, and the complex behaviours of merging glaciers. Such processes can be especially complicated in topographically constrained glacier complexes such as the former AIF. For instance, when two glaciers converge, their respective ice masses will become separated by a suture zone sometimes visible through formation of medial moraines (Small et al., 1979). Reconstructing the precise locations and, importantly, the lateral migrations of such suture zones in paleo glaciers, which result from disequilibrium in the magnitudes of confronting driving stresses from two glaciers, can be crucial to explain: 1) the formation of specific subglacial landforms and their locations (e.g. lineations, drumlins and their orientations), 2) the lack or instead over-abundance of ice-contact deposits in specific locations, or 3) the puzzling provenances of specific sediments deposited at glacier margins. While such complex ice dynamics can be well-represented in glacier evolution models solving high-order ice-flow physics, particle tracking offers a means to easily visualize and quantify these processes (otherwise invisible) in model outputs. Our Mont Salève case study (section 3.3.3) is a good example for which understanding the location and migration of the suture zone separating the Rhône and Arve glaciers, easily visible with particles on Figure 8 (panel a), is key in understanding the modelled provenance and transport pathways of specific ice-contact deposits in this region (e.g. the Mont Salève erratics).

4.2.3 Implications for research on glacial landscape evolution

By combining our results with those of Leger et al. (2025), we demonstrate that GPU-parallelization can substantially decrease the computational cost of glacier evolution modelling coupled with Lagrangian particle tracking (Fig. 4). Besides helping to estimate glacial sediment transport trajectories over multi-millennial and continental spatio-temporal scales, we believe this new approach opens the door to a range of earth-surface modelling capabilities that may prove useful in addressing research questions in the fields of glaciology and mountain geomorphology. As an example, we believe there is potential for future model-data comparison studies to better characterize the role of glacial erosion on the relief development of mountain belts during Quaternary glaciations (e.g. Bernard et al., 2025), but also on more contemporary timescales (e.g. Delaney et al., 2023). Open questions remain, for instance, regarding the relative proportions of glacial erosion materials evacuated as glaciofluvial bed/suspended load versus frozen-on englacial debris, their role in controlling sediment export and deposition rates in the lowlands, and the spatio-temporal variability of these different processes under changing hydro-climatic conditions (Alley et al., 1998; Zhang et al., 2022; Fedotova & Magnani, 2024; Delaney et al., *in press*). Large uncertainties remain also regarding subglacial mechanisms of sediment storage and resulting shielding of bedrock erosion, introducing sediment evacuation delays that are challenging to quantify, and which may bias current understandings of subglacial erosion's correlation with basal glacier conditions including ice velocity and temperature (Herman et al., 2021; Delaney & Anderson, 2022). These challenging questions would benefit from new model-data comparison studies that bridge spatio-temporal gaps in empirical

observations, thus making more holistic and fully coupled model frameworks involving particle tracking valuable tools for future investigations addressing these questions (Delaney et al., 2023).

To this day, one of the most advanced and efficient models coupling glacier-flow simulations with processes of fluvial and hillslope erosion, subglacial erosion, subglacial hydrology, and sediment transport over multi-millennial timescales, is the integrated second-order shallow ice approximation model (iSOSIA; Egholm et al., 2011). However, it remains computationally unfeasible to run such a CPU-based model over entire mountain ranges (e.g. the Alps), Quaternary-glaciation timescales (10^4-10^6 yr), and at the high spatial resolutions (<500 m) required to accurately resolve steep mountain topographies (Bernard et al., 2025). On the other hand, recent advances in GPU-optimized modelling and physics-informed machine learning have enabled to overcome such computational bottlenecks whilst in some cases respecting high-order 3D physics (e.g. Jouvet & Cordonnier, 2023; Cordonnier et al., 2023; Jain et al., 2024; Leger et al., 2025). The efficient GPU-parallelization of Lagrangian tracking will enable incorporating end-to-end advection of large particle numbers within fully coupled glacier-and-landscape evolution models. Therefore, it seems plausible that over the next few years, GPU-based modelling approaches permit high-resolution simulations whose outputs can be directly compared against empirical data on, for instance, Quaternary glacier incision rates and timing (e.g. Valla et al., 2011) or sediment export volumes and provenance data (e.g. Herman et al., 2015; Koppes et al., 2015; Overeem et al., 2017). Such model-data comparisons may shed light on the complex mechanisms influencing the dynamics of glacial erosion and its interaction with climate and topographic change over various spatio-temporal scales.

5. Conclusion

This study presents the first modelling reconstruction of sediment transport by glaciers across the entire European Alps during the Last Glacial Maximum (LGM). This is achieved via the new coupling of 3D Lagrangian particle tracking within the Graphics Processing Units (GPU)-accelerated, high-resolution glacier simulations of Leger et al. (2025) using the Instructed Glacier Model (IGM). Our modelling computes the 3D ice advection of tens of millions of particles, enabling us to simulate complex, time-transient glacial sediment transport trajectories across the Alps over multi-millennial timescales (40-18 ka), and at an unprecedentedly high spatial resolution (300 m). Here, a key methodological innovation is the development of process-based particle seeding schemes for both subglacial and supraglacial sediment origins over large spatial scales, attempting to capture distinct erosion and debris entrainment dynamics. Our GPU-based approach significantly reduces the computational cost of Lagrangian tracking, making it

1408 feasible to track tens of millions of particles within glacier evolution models ran over continental domains, which represents a computational breakthrough for glacial sediment modelling.

1410 Our two complementary sets of results, i.e. the sink-to-source (reconstructing ice-contact deposit provenance) and source-to-sink (mapping potential depositional locations) analyses, yield Alps-wide
1412 estimates of LGM glacial sediment routing, transport times, erosion timing, and cumulative ice-free exposure. The full results of these analyses are presented in two catalogues accessible via the Zenodo
1414 repository attached to this publication. We find particles of supraglacial origin are typically eroded earlier in time (i.e. are older), experience longer glacier residence times, and more cumulative ice-free exposure,
1416 with implications for interpreting cosmogenic nuclide inheritance signals in surface exposure dating for instance.

1418

By presenting case studies such as the Mont Salève erratics transport histories, we also show how our
1420 modelling can address empirical hypotheses by reconstructing detailed particle trajectories consistent with known lithologies, which can in certain cases suggest revised paleo ice-flow interpretations. After
1422 comparing model results against empirical data, we find that sediment trajectories overlap with dated erratic boulders in 81-68% of cases, supporting the reliability of the approach and validating the use of
1424 process-based particle seeding schemes over simpler methods. Furthermore, our results enable us to precisely detect and map multiple LGM ice transfluences, including previously unreported overflow
1426 pathways, and estimate their occurrence durations, thus offering new perspectives on complex internal ice-flow and topographically uncoupled glacier dynamics across the Alps.

1428

We believe this first Alps-wide modelling of LGM glacial sediment transport and ice-flow dynamics
1430 provides a range of predictions that will prove useful to glacial geologists, geomorphologists, sedimentologists and industries studying ice-contact sediments related to Late-Quaternary glaciations of
1432 the European Alps. Finally, the computationally efficient (GPU-based) coupled glacier-particle modelling framework developed here opens new avenues for quantitative model-data comparisons using preserved
1434 glacial geomorphology and provides a powerful tool to study and better constrain paleo ice dynamics, sediment provenance, and Quaternary glacial landscape evolution.

1436

1438

1440

1442

Code and data availability.

The data that represent the main findings of this study: namely the 'sink-to-source', 'source-to-sink', 'ice-transfluence' data catalogues and their corresponding particle-trajectory polyline shapefiles are available from the following Zenodo open-access online repository: https://doi.org/10.5281/zenodo.18374156. This repository also features a series of videos displaying Alps-wide results from our Instructed Glacier Model (IGM) simulations including the visual rendering of particle advection and deposition for both subglacial and supraglacial seeding and zoomed in for 10 different regions of the Alps. These videos are also accessible via the IGM YouTube channel: https://www.youtube.com/@IGMGlacierModel/playlists. Finally, this repository also features codes, files and detailed instructions required to reproduce this study's specific IGM simulations using the correct IGM version (2.2.1.). Note that whilst the full modelled particle database produced in this study is too large to be stored online and shared (~1.22 TB), readers are encouraged to contact the corresponding author if wishing to compute and display particle trajectories for specific sinks or sources.

The IGM source code (Python programming language) which now includes the fully GPU-optimized particle-tracking module (in IGM versions ≥2.2.3) is open access and available from the GitHub repository at https://github.com/instructed-glacier-model/igm.git. IGM's documentation is available from its official website at https://igm-model.org/.

Supplement.

The supplement related to this article is available online at: ………..

Author contributions.

T.P.M.L., G.J., and M.B. conceived and designed the study with input ideas from S.K., A.V., A.H., F.H. and S.N. G.J. developed the original version of IGM, including the Lagrangian particle-tracking module in IGM, whose code was then modified and improved by B.F. within the context of this study to become fully GPU-optimised, with tests and compute-time diagnostics from T.P.M.L. T.P.M.L. designed and coded the particle seeding schemes and carried out the IGM simulations. T.P.M.L. created the post-processing coding workflow for particle trajectory extraction and mapping, with help from B.A. who optimized the Python code for efficient search of the large output particle database. T.P.M.L. compiled and generated the hydrological basin, ice-contact deposit, and surface lithology databases required for running the 'sink-to-source' and 'source-to-sink' analyses presented above. S.K. contributed to the extraction and mapping of certain surface lithologies. T.P.M.L. conducted the model-data comparison against erratic boulder data leveraging prior literature data mining and exposure-age recalculations from S.K. T.P.M.L. ran model sensitivity analyses, wrote the manuscript, and produced all figures and supplementary materials. All co-authors contributed to the discussions, interpretations and gave feedback on the final manuscript and figures.

1498

1500

1502

1504

1506

1508

1510

1512

References

1516   Aaron, J.: ORIN-3D – A new model for efficient simulation of landslide motion on a GPU using CUDA, Comput. Geotech., 153, 105078, https://doi.org/10.1016/j.compgeo.2022.105078, 2023.

1518   Agassiz, L.: Études sur les glaciers, Aux frais de l'auteur. En commission chez Jent et Gassmann, libraires., Soleure, https://doi.org/https://doi.org/10.1017/CBO9781139235877, 1840.

1520   Alley, R. B., Cuffey, K. M., Evenson, E. B., Strasser, J. C., Lawson, D. E., and Larson, G. J.: How glaciers entrain and transport basal sediment: Physical constraints, Quat. Sci. Rev., 16, 1017–1038, https://doi.org/10.1016/S0277-
1522   3791(97)00034-6, 1997.

        Alley, R. B., Lawson, D. E., Evenson, E. B., Strasser, J. C., and Larson, G. J.: Glaciohydraulic supercooling: a
1524   freeze-on mechanism to create stratified, debris-rich basal ice: II. Theory, Journal of Glaciology, 44, 563–569, https://doi.org/10.3189/S0022143000002070, 1998.

1526   Archer, R. E., Ely, J. C., Heaton, T. J., Butcher, F. E. G., Hughes, A. L. C., and Clark, C. D.: Assessing ice sheet models against the landform record: The Likelihood of Accordant Lineations Analysis (LALA) tool, Earth Surf.
1528   Process. Landf., 48, 2754–2771, https://doi.org/10.1002/esp.5658, 2023.

        Aschwanden, A., Bueler, E., Khroulev, C., and Blatter, H.: An enthalpy formulation for glaciers and ice sheets,
1530   Journal of Glaciology, 58, 441–457, https://doi.org/10.3189/2012JoG11J088, 2012.

        Benn, D. I., Bolch, T., Hands, K., Gulley, J., Luckman, A., Nicholson, L. I., Quincey, D., Thompson, S., Toumi,
1532   R., and Wiseman, S.: Response of debris-covered glaciers in the Mount Everest region to recent warming, and implications for outburst flood hazards, Earth. Sci. Rev., 114, 156–174,
1534   https://doi.org/10.1016/j.earscirev.2012.03.008, 2012.

        Bernard, M., Steer, P., Gallagher, K., and Lundbek Egholm, D.: Modelling the effects of ice transport and
1536   sediment sources on the form of detrital thermochronological age probability distributions from glacial settings, Earth Surface Dynamics, 8, 931–953, https://doi.org/10.5194/esurf-8-931-2020, 2020.

1538   Bernard, M., van der Beek, P. A., Pedersen, V. K., and Colleps, C.: Production and Preservation of Elevated Low-Relief Surfaces in Mountainous Landscapes by Pliocene-Quaternary Glaciations, AGU Advances, 6,
1540   https://doi.org/10.1029/2024AV001610, 2025.

        Bichler, M. G., Reindl, M., Reitner, J. M., Drescher-Schneider, R., Wirsig, C., Christl, M., Hajdas, I., and Ivy-
1542   Ochs, S.: Landslide deposits as stratigraphical markers for a sequence-based glacial stratigraphy: a case study of a Younger Dryas system in the Eastern Alps, Boreas, 45, 537–551, https://doi.org/10.1111/bor.12173, 2016.

1544   Bigi, G., Castellarin, A., Coli, M., Dal Piaz, G. V., Sartori, R., Scandone, P., and Vai, G.: Structural Model of Italy scale 1:500,000, sheet 1, Florence, 1990a.

1546   Bigi, G., Castellarin, A., Coli, M., Dal Piaz, G. V., and Vai, G.: Structural Model of Italy scale 1:500,000, sheet 2, Florence, 1990b.

1548   Blatter, H.: Velocity and stress fields in grounded glaciers: a simple algorithm for including deviatoric stress gradients, Journal of Glaciology, 41, 333–344, https://doi.org/10.3189/S002214300001621X, 1995.

1550   Boulton, G. S.: Boulder shapes and grain-size distributions of debris as indicators of transport paths through a glacier and till genesis, Sedimentology, 25, 773–799, https://doi.org/10.1111/j.1365-3091.1978.tb00329.x, 1978.

1552   Boulton, G. S.: Processes of Glacier Erosion on Different Substrata, Journal of Glaciology, 23, 15–38, https://doi.org/10.3189/S0022143000029713, 1979.

1554   Boulton, G. S.: Theory of glacial erosion, transport and deposition as a consequence of subglacial sediment deformation, Journal of Glaciology, 42, 43–62, https://doi.org/10.3189/S0022143000030525, 1996.

1556   Boxleitner, M., Ivy-Ochs, S., Egli, M., Brandova, D., Christl, M., and Maisch, M.: Lateglacial and Early Holocene
       glacier stages - New dating evidence from the Meiental in central Switzerland, Geomorphology, 340, 15–31,
1558   https://doi.org/10.1016/j.geomorph.2019.04.004, 2019.

       Braakhekke, J., Ivy-Ochs, S., Monegato, G., Gianotti, F., Martin, S., Casale, S., and Christl, M.: Timing and flow
1560   pattern of the Orta Glacier (European Alps) during the Last Glacial Maximum, Boreas, 49, 315–332,
       https://doi.org/10.1111/bor.12427, 2020.

1562   Bueler, E. and van Pelt, W.: Mass-conserving subglacial hydrology in the Parallel Ice Sheet Model version 0.6,
       Geosci. Model Dev., 8, 1613–1635, https://doi.org/10.5194/gmd-8-1613-2015, 2015.

1564   Buoncristiani, J.-F. and Campy, M.: Quaternary Glaciations in the French Alps and Jura, in: Quaternary
       Glaciations - Extent and Chronology - a closer look, vol. 15, edited by: Ehlers, J., Gibbard, P. L., and Hughes, P.
1566   D., 117–126, https://doi.org/10.1016/B978-0-444-53447-7.00010-6, 2011.

       Bussien Grosjean, D., Meisser, N., May-Leresche, S., Ulianov, A., and Vonlanthen, P.: The Morcles microgranite
1568   (Aiguilles Rouges, Swiss Alps): geochronological and geochemical evidences for a common origin with the
       Vallorcine intrusion, Swiss J. Geosci., 111, 35–49, https://doi.org/10.1007/s00015-017-0282-3, 2018.

1570   Byers, J., Cohen, D., and Iverson, N. R.: Subglacial clast/bed contact forces, Journal of Glaciology, 58, 89–98,
       https://doi.org/10.3189/2012JoG11J126, 2012.

1572   Calov, R. and Greve, R.: A semi-analytical solution for the positive degree-day model with stochastic temperature
       variations, Journal of Glaciology, 51, 173–175, https://doi.org/10.3189/172756505781829601, 2005.

1574   Campy, M.: Palaeogeographical relationships between Alpine and Jura glaciers during the two last Pleistocene
       glaciations, Palaeogeogr. Palaeoclimatol. Palaeoecol., 93, 1–12, https://doi.org/10.1016/0031-0182(92)90180-D,
1576   1992.

       Capuzzo, N., Handler, R., Neubauer, F., and Wetzel, A.: Post-collisional rapid exhumation and erosion during
1578   continental sedimentation: the example of the late Variscan Salvan-Dorénaz basin (Western Alps), International
       Journal of Earth Sciences, 92, 364–379, https://doi.org/10.1007/s00531-003-0332-0, 2003.

1580   Champel, B., van der Beek, P., Mugnier, J., and Leturmy, P.: Growth and lateral propagation of fault-related folds
       in the Siwaliks of western Nepal: Rates, mechanisms, and geomorphic signature, J. Geophys. Res. Solid Earth,
1582   107, https://doi.org/10.1029/2001JB000578, 2002.

       Clark, C. D., Ely, J. C., Greenwood, S. L., Hughes, A. L. C., Meehan, R., Barr, I. D., Bateman, M. D., Bradwell,
1584   T., Doole, J., Evans, D. J. A., Jordan, C. J., Monteys, X., Pellicer, X. M., and Sheehy, M.: BRITICE Glacial Map,
       version 2: a map and GIS database of glacial landforms of the last British–Irish Ice Sheet, Boreas, 47, 11-e8,
1586   https://doi.org/10.1111/bor.12273, 2018.

       Clark, C. D., Ely, J. C., Hindmarsh, R. C. A., Bradley, S., Ignéczi, A., Fabel, D., Ó Cofaigh, C., Chiverrell, R. C.,
1588   Scourse, J., Benetti, S., Bradwell, T., Evans, D. J. A., Roberts, D. H., Burke, M., Callard, S. L., Medialdea, A.,
       Saher, M., Small, D., Smedley, R. K., Gasson, E., Gregoire, L., Gandy, N., Hughes, A. L. C., Ballantyne, C.,
1590   Bateman, M. D., Bigg, G. R., Doole, J., Dove, D., Duller, G. A. T., Jenkins, G. T. H., Livingstone, S. L.,
       McCarron, S., Moreton, S., Pollard, D., Praeg, D., Sejrup, H. P., Van Landeghem, K. J. J., and Wilson, P.: Growth
1592   and retreat of the last British–Irish Ice Sheet, 31 000 to 15 000 years ago: the BRITICE-CHRONO reconstruction,
       Boreas, 51, 699–758, https://doi.org/10.1111/bor.12594, 2022.

1594   Cogez, A., Herman, F., Pelt, É., Reuschlé, T., Morvan, G., Darvill, C. M., Norton, K. P., Christl, M., Märki, L.,
       and Chabaux, F.: U-Th and 10Be constraints on sediment recycling in proglacial settings, Lago Buenos Aires,
1596   Patagonia, Earth Surface Dynamics, 6, 121–140, https://doi.org/10.5194/esurf-6-121-2018, 2018.

       Cook, S. J., Swift, D. A., Kirkbride, M. P., Knight, P. G., and Waller, R. I.: The empirical basis for modelling
1598   glacial erosion rates, Nat. Commun., 11, 1–7, https://doi.org/10.1038/s41467-020-14583-8, 2020.

Cordonnier, G., Jouvet, G., Peytavie, A., Braun, J., Cani, M.-P., Benes, B., Galin, E., Guérin, E., and Gain, J.: Forming Terrains by Glacial Erosion, ACM Trans. Graph., 42, 1–14, https://doi.org/10.1145/3592422, 2023.

Coutterand, S.: Étude géomophologique des flux glaciaires dans les Alpes nord-occidentales au Pléistocène récent. Du maximum de la dernière glaciation aux premières étapes de la déglaciation., PhD thesis, Université de Savoie, Le Bourget du Lac, 1–468 pp., 2010.

Coutterand, S.: Origines des blocs erratiques du Salève, Arch. Sci., 70, 51–56, 2018.

Cuffey, K. M. and Patterson, W. S. B.: The physics of glaciers, Academic Press, 1–704 pp., 2010.

Davies, B. J., Roberts, D. H., Bridgland, D. R., Ó Cofaigh, C., Riding, J. B., Demarchi, B., Penkman, K. E. H., and Pawley, S. M.: Timing and depositional environments of a Middle Pleistocene glaciation of northeast England: New evidence from Warren House Gill, County Durham, Quat. Sci. Rev., 44, 180–212, https://doi.org/10.1016/j.quascirev.2010.02.003, 2012.

Davies, B. J., Darvill, C. M., Lovell, H., Bendle, J. M., Dowdeswell, J. A., Fabel, D., García, J.-L., Geiger, A., Glasser, N. F., Gheorghiu, D. M., Harrison, S., Hein, A. S., Kaplan, M. R., Martin, J. R. V., Mendelova, M., Palmer, A., Pelto, M., Rodés, Á., Sagredo, E. A., Smedley, R. K., Smellie, J. L., and Thorndycraft, V. R.: The evolution of the Patagonian Ice Sheet from 35 ka to the present day (PATICE), Earth. Sci. Rev., 204, 103152, https://doi.org/10.1016/j.earscirev.2020.103152, 2020.

Delaney, I. and Anderson, L. S.: Debris Cover Limits Subglacial Erosion and Promotes Till Accumulation, Geophys. Res. Lett., 49, https://doi.org/10.1029/2022GL099049, 2022.

Delaney, I., Anderson, L., and Herman, F.: Modeling the spatially distributed nature of subglacial sediment transport and erosion, Earth Surface Dynamics, 11, 663–680, https://doi.org/10.5194/esurf-11-663-2023, 2023.

Dielforder, A. and Hetzel, R.: The deglaciation history of the Simplon region (southern Swiss Alps) constrained by 10Be exposure dating of ice-molded bedrock surfaces, Quat. Sci. Rev., 84, 26–38, https://doi.org/10.1016/j.quascirev.2013.11.008, 2014.

Duprat-Oualid, F., Rius, D., Bégeot, C., Magny, M., Millet, L., Wulf, S., and Appelt, O.: Vegetation response to abrupt climate changes in Western Europe from 45 to 14.7k cal a BP: the Bergsee lacustrine record (Black Forest, Germany), J. Quat. Sci., 32, 1008–1021, https://doi.org/10.1002/jqs.2972, 2017.

Egholm, D. L., Knudsen, M. F., Clark, C. D., and Lesemann, J. E.: Modeling the flow of glaciers in steep terrains: The integrated second-order shallow ice approximation (iSOSIA), J. Geophys. Res. Earth Surf., 116, https://doi.org/10.1029/2010JF001900, 2011.

Ehlers, J., Gibbard, P. L., and Hughes, P. D.: Developments in quaternary sciences: quaternary glaciations-extent and chronology: a closer look, 1st ed., edited by: Ehlers, J., Gibbard, P. L., and Hughes, P. D., Elsevier, Amsterdam, 2–1118 pp., 2011.

Ely, J. C., Clark, C. D., Small, D., and Hindmarsh, R. C. A.: ATAT 1.1, the Automated Timing Accordance Tool for comparing ice-sheet model output with geochronological data, Geosci. Model Dev., 12, 933–953, https://doi.org/10.5194/gmd-12-933-2019, 2019.

Enkelmann, E. and Ehlers, T. A.: Evaluation of detrital thermochronology for quantification of glacial catchment denudation and sediment mixing, Chem. Geol., 411, 299–309, https://doi.org/10.1016/j.chemgeo.2015.07.018, 2015.

Esmark, J.: Bidrag til vor Jordklodes Historie, Magazin for Naturvidenskaberne, 2, 28–49, 1824.

Evans, D. J. A. and Benn, D. I.: A Practical Guide to the Study of Glacial Sediments, Routledge, 2004.

Evans, D. J. A., Phillips, E. R., Hiemstra, J. F., and Auton, C. A.: Subglacial till: Formation, sedimentary characteristics and classification, Earth. Sci. Rev., 78, 115–176, https://doi.org/10.1016/j.earscirev.2006.04.001, 2006.

1642 Federici, P. R., Ribolini, A., and Spagnolo, M.: Glacial history of the Maritime Alps from the Last Glacial
      Maximum to the Little Ice Age, Geological Society, London, Special Publications, 433, 137–159,
1644 https://doi.org/10.1144/SP433.9, 2017.

      Fedotova, A. and Magnani, M. B.: Glacial Erosion Rates Since the Last Glacial Maximum for the Former
1646 Argentino Glacier and Present-Day Upsala Glacier, Patagonia, J. Geophys. Res. Earth Surf., 129,
      https://doi.org/10.1029/2024JF007960, 2024.

1648 Fischer, L., Purves, R. S., Huggel, C., Noetzli, J., and Haeberli, W.: On the influence of topographic, geological
      and cryospheric factors on rock avalanches and rockfalls in high-mountain areas, Natural Hazards and Earth
1650 System Sciences, 12, 241–254, https://doi.org/10.5194/nhess-12-241-2012, 2012.

      Fischer, U. H., Bebiolka, A., Brandefelt, J., Follin, S., Hirschorn, S., Jensen, M., Keller, S., Kennell, L., Näslund,
1652 J.-O., Normani, S., Selroos, J.-O., and Vidstrand, P.: Radioactive Waste Under Conditions of Future Ice Ages, in:
      Snow and Ice-Related Hazards, Risks, and Disasters, edited by: Shroder, J. F., Haeberli, W., and Whiteman, C.,
1654 Elsevier, Boston, 345–393, https://doi.org/10.1016/B978-0-12-394849-6.00011-1, 2015.

      Fischer, U. H., Bebiolka, A., Brandefelt, J., Cohen, D., Harper, J., Hirschorn, S., Jensen, M., Kennell, L., Liakka,
1656 J., Näslund, J.-O., Normani, S., Stück, H., and Weitkamp, A.: Radioactive waste under conditions of future ice
      ages, in: Snow and Ice-Related Hazards, Risks, and Disasters, edited by: Haeberli, W. and Whiteman, C., Elsevier,
1658 323–375, https://doi.org/10.1016/B978-0-12-817129-5.00005-6, 2021.

      Florineth, D. and Schlüchter, C.: Reconstructing the Last Glacial Maximum (LGM) ice surface geometry and
1660 flowlines in the Central Swiss Alps, Eclogae Geologicae Helvetiae, 91, https://doi.org/10.5169/seals-168431,
      1998.

1662 Gallach, X., Perrette, Y., Lafon, D., Chalmin, É., Deline, P., Ravanel, L., Carcaillet, J., and Wallet, T.: A new
      method for dating the surface exposure age of granite rock walls in the Mont Blanc massif by reflectance
1664 spectroscopy, Quat. Geochronol., 64, 101–156, https://doi.org/10.1016/j.quageo.2021.101156, 2021.

      Geikie, J.: The Alps during the Glacial Period, Bulletin of the American Geographical Society, 42, 192,
1666 https://doi.org/10.2307/200422, 1910.

      Geologische Bundesanstalt Österreich: Geodaten - Blatt 197 Kötschach (1:50.000), Tethys RDR, Geologische
1668 Bundesanstalt (GBA), Wien, https://doi.org/https://doi.org/10.24341/tethys.90, 2021a.

      Geologische Bundesanstalt Österreich: Geodaten - Blatt 198 Weißbriach (1:50.000), Tethys RDR, Geologische
1670 Bundesanstalt (GBA), Wien, https://doi.org/https://doi.org/10.24341/tethys.88, 2021b.

      Gianotti, F., Forno, M. G., Ivy-Ochs, S., and Kubik, P. W.: New chronological and stratigraphical data on the Ivrea
1672 amphitheatre (Piedmont, NW Italy), Quaternary International, 190, 123–135,
      https://doi.org/10.1016/j.quaint.2008.03.001, 2008.

1674 Gianotti, F., Forno, M. G., Ajassa, R., Cámara, F., Costa, E., Ferrando, S., Giardino, M., Lucchesi, S., Motta, L.,
      Motta, M., Perotti, L., and Rossetti, P.: The Ivrea Morainic Amphitheatre as a Well Preserved Record of the
1676 Quaternary Climate Variability (PROGEO-Piemonte Project, NW Italy), in: Engineering Geology for Society and
      Territory - Volume 8, edited by: Lollino Giorgio and Giordan, D. and M. C. and C. B. and Y. I. and M. C.,
1678 Springer International Publishing, Cham, 235–238, https://doi.org/10.1007/978-3-319-09408-3_39, 2015.

      Gibbons, A. B., Megeath, Joe. D., and Pierce, K. L.: Probability of moraine survival in a succession of glacial
1680 advances, Geology, 12, 327, https://doi.org/10.1130/0091-7613(1984)12<327:POMSIA>2.0.CO;2, 1984.

      Glasser, N. and Jansson, K.: The Glacial map of southern South America, J. Maps, 4, 175–196,
1682 https://doi.org/10.4113/jom.2008.1020, 2008.

      Graf, A., Akçar, N., Ivy-Ochs, S., Strasky, S., Kubik, P. W., Christl, M., Burkhard, M., Wieler, R., and Schlüchter,
1684 C.: Multiple advances of Alpine glaciers into the Jura Mountains in the Northwestern Switzerland, Swiss J.
      Geosci., 108, 225–238, https://doi.org/10.1007/s00015-015-0195-y, 2015.

1686   Guillon, H., Mugnier, J., Buoncristiani, J., Carcaillet, J., Godon, C., Prud'homme, C., van der Beek, P., and
        Vassallo, R.: Improved discrimination of subglacial and periglacial erosion using 10Be concentration
1688   measurements in subglacial and supraglacial sediment load of the Bossons glacier (Mont Blanc massif, France),
        Earth Surf. Process. Landf., 40, 1202–1215, https://doi.org/10.1002/esp.3713, 2015.

1690   Hallet, B.: Glacial Abrasion and Sliding: their Dependence on the Debris Concentration in Basal Ice, Ann.
        Glaciol., 2, 23–28, https://doi.org/10.3189/172756481794352487, 1981.

1692   Herman, F., Beyssac, O., Brughelli, M., Lane, S. N., Leprince, S., Adatte, T., Lin, J. Y. Y., Avouac, J.-P., and Cox,
        S. C.: Erosion by an Alpine glacier, Science (1979)., 350, 193–195, https://doi.org/10.1126/science.aab2386,
1694   2015.

        Herman, F., De Doncker, F., Delaney, I., Prasicek, G., and Koppes, M.: The impact of glaciers on mountain
1696   erosion, Nat. Rev. Earth Environ., 2, 422–435, https://doi.org/10.1038/s43017-021-00165-9, 2021.

        Heyman, J., Stroeven, A. P., Harbor, J. M., and Caffee, M. W.: Too young or too old: Evaluating cosmogenic
1698   exposure dating based on an analysis of compiled boulder exposure ages, Earth Planet. Sci. Lett., 302, 71–80,
        https://doi.org/10.1016/j.epsl.2010.11.040, 2011.

1700   Hughes, A. L. C., Clark, C. D., and Jordan, C. J.: Subglacial bedforms of the last British Ice sheet, J. Maps, 6,
        543–563, https://doi.org/10.4113/jom.2010.1111, 2010.

1702   Humlum, O.: Changes in Texture and Fabric of Particles in Glacial Traction with Distance from Source,
        Mỳrdalsjökull, Iceland, Journal of Glaciology, 31, 150–156, https://doi.org/10.3189/S0022143000006390, 1985.

1704   Humphrey, N. F. and Raymond, C. F.: Hydrology, erosion and sediment production in a surging glacier:
        Variegated Glacier, Alaska, 1982–83, Journal of Glaciology, 40, 539–552,
1706   https://doi.org/10.3189/S0022143000012429, 1994.

        van Husen, D.: LGM and late-glacial fluctuations in the Eastern Alps, Quaternary International, 38–39, 109–118,
1708   https://doi.org/10.1016/S1040-6182(96)00017-1, 1997.

        Iverson, N. R., Hanson, B., Hooke, R. LeB., and Jansson, P.: Flow Mechanism of Glaciers on Soft Beds, Science
1710   (1979)., 267, 80–81, https://doi.org/10.1126/science.267.5194.80, 1995.

        Iverson, N. R., Cohen, D., Hooyer, T. S., Fischer, U. H., Jackson, M., Moore, P. L., Lappegard, G., and Kohler, J.:
1712   Effects of Basal Debris on Glacier Flow, Science (1979)., 301, 81–84, https://doi.org/10.1126/science.1083086,
        2003.

1714   Ivy-Ochs, S.: Glacier variations in the European Alps at the end of the last glaciation, Cuadernos de Investigación
        Geográfica, 41, 295–315, https://doi.org/10.18172/cig.2750, 2015.

1716   Ivy-Ochs, S., Schäfer, J., Kubik, P. W., Synal, H. A., and Schlüchter, C.: Timing of deglaciation on the northern
        Alpine foreland (Switzerland), Eclogae Geologicae Helvetiae, 97, 47–55, https://doi.org/10.1007/s00015-004-
1718   1110-0, 2004.

        Ivy-Ochs, S., Lucchesi, S., Baggio, P., Fioraso, G., Gianotti, F., Monegato, G., Graf, A. A., Akçar, N., Christl, M.,
1720   Carraro, F., Forno, M. G., and Schlüchter, C.: New geomorphological and chronological constraints for glacial
        deposits in the Rivoli-Avigliana end-moraine system and the lower Susa Valley (Western Alps, NW Italy), J. Quat.
1722   Sci., 33, 550–562, https://doi.org/10.1002/jqs.3034, 2018.

        Ivy-Ochs, S., Monegato, G., and Reitner, J. M.: The Alps: glacial landforms from the Last Glacial Maximum, in:
1724   European Glacial Landscapes, edited by: Palacios, D., Hughes, P. D., García-Ruiz, J. M., and Andrés, N., Elsevier,
        449–460, https://doi.org/10.1016/B978-0-12-823498-3.00030-3, 2022.

1726   Jain, A., Kerbl, B., Gain, J., Finley, B., and Cordonnier, G.: FastFlow: GPU Acceleration of Flow and Depression
        Routing for Landscape Simulation, Computer Graphics Forum, 43, https://doi.org/10.1111/cgf.15243, 2024.

1728 Jouvet, G. and Cordonnier, G.: Ice-flow model emulator based on physics-informed deep learning, Journal of
Glaciology, 1–15, https://doi.org/10.1017/jog.2023.73, 2023.

1730 Jouvet, G., Seguinot, J., Ivy-ochs, S., and Funk, M.: Modelling the diversion of erratic boulders by the Valais
Glacier during the last glacial maximum, Journal of Glaciology, 63, 487–498, https://doi.org/10.1017/jog.2017.7,
1732 2017.

Jouvet, G., Cordonnier, G., Kim, B., Lüthi, M., Vieli, A., and Aschwanden, A.: Deep learning speeds up ice flow
1734 modelling by several orders of magnitude, Journal of Glaciology, 68, 651–664,
https://doi.org/10.1017/jog.2021.120, 2022.

1736 Jouvet, G., Cohen, D., Russo, E., Buzan, J., Raible, C. C., Haeberli, W., Kamleitner, S., Ivy-Ochs, S., Imhof, M.
A., Becker, J. K., Landgraf, A., and Fischer, U. H.: Coupled climate-glacier modelling of the last glaciation in the
1738 Alps, Journal of Glaciology, 1–15, https://doi.org/10.1017/jog.2023.74, 2023.

Kamleitner, S., Ivy-Ochs, S., Monegato, G., Gianotti, F., Akçar, N., Vockenhuber, C., Christl, M., and Synal, H.-
1740 A.: The Ticino-Toce glacier system (Swiss-Italian Alps) in the framework of the Alpine Last Glacial Maximum,
Quat. Sci. Rev., 279, 107400, https://doi.org/10.1016/j.quascirev.2022.107400, 2022.

1742 Kamleitner, S., Ivy-Ochs, S., Manatschal, L., Akçar, N., Christl, M., Vockenhuber, C., Hajdas, I., and Synal, H.-
A.: Last Glacial Maximum glacier fluctuations on the northern Alpine foreland: Geomorphological and
1744 chronological reconstructions from the Rhine and Reuss glacier systems, Geomorphology, 423, 108548,
https://doi.org/10.1016/j.geomorph.2022.108548, 2023.

1746 Kamleitner, S., Leger, T. P. M., Ivy-Ochs, S., Nussbaumer, S. U., Vieli, A., and Jouvet, G.: AlpIce - Towards an
Alps-wide database of empirical geo(morpho)logical and geochronological data constraining Last Glacial
1748 Maximum to Holocene glacier fluctuations, in: EGU General Assembly 2024, https://doi.org/10.5194/egusphere-
egu24-9282, 2024a.

1750 Kamleitner, S., Ivy-Ochs, S., Salcher, B., and Reitner, J. M.: Reconstructing basal ice flow patterns of the Last
Glacial Maximum Rhine glacier (northern Alpine foreland) based on streamlined subglacial landforms, Earth
1752 Surf. Process. Landf., 49, 746–769, https://doi.org/10.1002/esp.5733, 2024b.

Keller, O. and Krayss, E.: Mittel- und spätpleistozäne Stratigraphie und Morphogenese in Schlüsselregionen der
1754 Nordschweiz, E&G Quaternary Science Journal, 59, 88–119, https://doi.org/10.3285/eg.59.1-2.08, 2011.

Kelly, M. A., Buoncristiani, J.-F., and Schlüchter, C.: A reconstruction of the last glacial maximum (LGM) ice-
1756 surface geometry in the western Swiss Alps and contiguous Alpine regions in Italy and France, Eclogae
Geologicae Helvetiae, 97, 57–75, https://doi.org/10.1007/s00015-004-1109-6, 2004.

1758 Koppes, M., Hallet, B., Rignot, E., Mouginot, J., Wellner, J. S., and Boldt, K.: Observed latitudinal variations in
erosion as a function of glacier dynamics, Nature, 526, 100–103, https://doi.org/10.1038/nature15385, 2015.

1760 Lane, S. N., Bakker, M., Gabbud, C., Micheletti, N., and Saugy, J.-N.: Sediment export, transient landscape
response and catchment-scale connectivity following rapid climate warming and Alpine glacier recession,
1762 Geomorphology, 277, 210–227, https://doi.org/10.1016/j.geomorph.2016.02.015, 2017.

Leger, T. P. M., Jouvet, G., Kamleitner, S., Mey, J., Herman, F., Finley, B. D., Ivy-Ochs, S., Vieli, A., Henz, A.,
1764 and Nussbaumer, S. U.: A data-consistent model of the last glaciation in the Alps achieved with physics-driven AI,
Nat. Commun., 16, 848, https://doi.org/10.1038/s41467-025-56168-3, 2025.

1766 Lehner, B. and Grill, G.: Global river hydrography and network routing: baseline data and new approaches to
study the world's large river systems, Hydrol. Process., 27, 2171–2186, https://doi.org/10.1002/hyp.9740, 2013.

1768 Letsch, D., Winkler, W., von Quadt, A., and Gallhofer, D.: The volcano-sedimentary evolution of a post-Variscan
intramontane basin in the Swiss Alps (Glarus Verrucano) as revealed by zircon U–Pb age dating and Hf isotope
1770 geochemistry, International Journal of Earth Sciences, 104, 123–145, https://doi.org/10.1007/s00531-014-1055-0,
2015.

1772   Linton, D. L.: Watershed Breaching by Ice in Scotland, Transactions and Papers (Institute of British Geographers), 1, https://doi.org/10.2307/621028, 1949.

1774   Luetscher, M., Boch, R., Sodemann, H., Spötl, C., Cheng, H., Edwards, R. L., Frisia, S., Hof, F., and Müller, W.: North Atlantic storm track changes during the Last Glacial Maximum recorded by Alpine speleothems, Nat.
1776   Commun., 6, 6344, https://doi.org/10.1038/ncomms7344, 2015.

Lyell, C.: On the geological evidence of the former existence of glaciers in Forfarshire, Proceedings of the
1778   Geological Society of London, 3, 337–345, 1840.

Manzotti, P.: Petro-structural map of the Dent Blanche tectonic system between Valpelline and Valtournenche
1780   valleys, Western Italian Alps, J. Maps, 7, 340–352, https://doi.org/10.4113/jom.2011.1179, 2011.

Margirier, A., Brondex, J., Rowan, A. V., Schmidt, C., Pedersen, V. K., Lehmann, B., Anderson, L. S., Veness, R.,
1782   Watson, C. S., Swift, D., and King, G. E.: Tracking Sediment Transport Through Miage Glacier, Italy, Using a Lagrangian Approach With Luminescence Rock Surface Burial Dating of Englacial Clasts, J. Geophys. Res. Earth
1784   Surf., 130, https://doi.org/10.1029/2024JF007773, 2025.

Matthews, J. A., Shakesby, R. A., and Fabel, D.: Very low inheritance in cosmogenic surface exposure ages of
1786   glacial deposits: A field experiment from two Norwegian glacier forelands, Holocene, 27, 1406–1414, https://doi.org/10.1177/0959683616687387, 2017.

1788   Mey, J., Scherler, D., Wickert, A. D., Egholm, D. L., Tesauro, M., Schildgen, T. F., and Strecker, M. R.: Glacial isostatic uplift of the European Alps, Nat. Commun., 7, 13382, https://doi.org/10.1038/ncomms13382, 2016.

1790   Mohammadi, M., McMackin, C., and Egli, M.: Source identification of morainic materials in soils of the Three Lakes region (Switzerland) using the fingerprinting technique, Catena (Amst)., 234, 107619,
1792   https://doi.org/10.1016/j.catena.2023.107619, 2024.

Monegato, G., Scardia, G., Hajdas, I., Rizzini, F., and Piccin, A.: The Alpine LGM in the boreal ice-sheets game,
1794   Sci. Rep., 7, 2078, https://doi.org/10.1038/s41598-017-02148-7, 2017.

Monegato, G., Kamleitner, S., Gianotti, F., Martin, S., Scapozza, C., and Ivy-Ochs, S.: The Ticino-Toce Ice
1796   Conveyor Belts During The Last Glacial Maximum, Alpine and Mediterranean Quaternary, 35, 119–134, https://doi.org/https://doi.org/10.26382/AMQ.2022.07, 2022.

1798   Moosdorf, N., Cohen, S., and von Hagke, C.: A global erodibility index to represent sediment production potential of different rock types, Applied Geography, 101, 36–44, https://doi.org/10.1016/j.apgeog.2018.10.010, 2018.

1800   Overeem, I., Hudson, B. D., Syvitski, J. P. M., Mikkelsen, A. B., Hasholt, B., van den Broeke, M. R., Noël, B. P. Y., and Morlighem, M.: Substantial export of suspended sediment to the global oceans from glacial erosion in
1802   Greenland, Nat. Geosci., 10, 859–863, https://doi.org/10.1038/ngeo3046, 2017.

Penck, A. and Brückner, E.: Die Alpen im Eiszeitalter, Tauchnitz, 1909.

1804   Preusser, F., Reitner, J. M., and Schlüchter, C.: Distribution, geometry, age and origin of overdeepened valleys and basins in the Alps and their foreland, Swiss J. Geosci., 103, 407–426, https://doi.org/10.1007/s00015-010-0044-y,
1806   2010.

Preusser, F., Graf, H. R., Keller, O., Krayss, E., and Schlüchter, C.: Quaternary glaciation history of northern
1808   Switzerland, E&G Quaternary Science Journal, 60, 282–305, https://doi.org/10.3285/eg.60.2-3.06, 2011.

Prud'homme, C., Vassallo, R., Crouzet, C., Carcaillet, J., Mugnier, J., and Cortés-Aranda, J.: Paired 10Be
1810   sampling of polished bedrock and erratic boulders to improve dating of glacial landforms: an example from the Western Alps, Earth Surf. Process. Landf., 45, 1168–1180, https://doi.org/10.1002/esp.4790, 2020.

1812   Ravazzi, C., Badino, F., Marsetti, D., Patera, G., and Reimer, P. J.: Glacial to paraglacial history and forest recovery in the Oglio glacier system (Italian Alps) between 26 and 15 ka cal BP, Quat. Sci. Rev., 58, 146–161,
1814   https://doi.org/10.1016/j.quascirev.2012.10.017, 2012.

1816   Reber, R., Akçar, N., Ivy-Ochs, S., Tikhomirov, D., Burkhalter, R., Zahno, C., Lüthold, A., Kubik, P. W.,
Vockenhuber, C., and Schlüchter, C.: Timing of retreat of the Reuss Glacier (Switzerland) at the end of the Last
Glacial Maximum, Swiss J. Geosci., 107, 293–307, https://doi.org/10.1007/s00015-014-0169-5, 2014.

1818   Reitner, J. M.: Glacial dynamics at the beginning of Termination I in the Eastern Alps and their stratigraphic
implications, Quaternary International, 164–165, 64–84, https://doi.org/10.1016/j.quaint.2006.12.016, 2007.

1820   Reitner, J. M., Gruber, W., Römer, A., and Morawetz, R.: Alpine overdeepenings and paleo-ice flow changes: an
integrated geophysical-sedimentological case study from Tyrol (Austria), Swiss J. Geosci., 103, 385–405,
1822   https://doi.org/10.1007/s00015-010-0046-9, 2010.

1824   Reynard, E.: Protecting stones: conservation of erratic blocks in Switzerland, in: Dimension stone, Taylor and
Francis, London, 3–7, 2004.

1826   Ribolini, A., Spagnolo, M., Cyr, A. J., and Federici, P. R.: Last Glacial Maximum and early deglaciation in the
Stura Valley, southwestern European Alps, Quat. Sci. Rev., 295, 107770,
https://doi.org/10.1016/j.quascirev.2022.107770, 2022.

1828   Roattino, T., Crouzet, C., Vassallo, R., Buoncristiani, J. F., Carcaillet, J., Gribenski, N., and Valla, P. G.:
Paleogeographical reconstruction of the western French Alps foreland during the last glacial maximum using
1830   cosmogenic exposure dating, Quaternary Research (United States), 111, 68–83,
https://doi.org/10.1017/qua.2022.25, 2023.

1832   Rowan, A. V., Egholm, D. L., Quincey, D. J., and Glasser, N. F.: Modelling the feedbacks between mass balance,
ice flow and debris transport to predict the response to climate change of debris-covered glaciers in the Himalaya,
1834   Earth Planet. Sci. Lett., 430, 427–438, https://doi.org/10.1016/j.epsl.2015.09.004, 2015.

1836   Russo, E., Buzan, J., Lienert, S., Jouvet, G., Velasquez Alvarez, P., Davis, B., Ludwig, P., Joos, F., and Raible, C.
C.: High-resolution LGM climate of Europe and the Alpine region using the regional climate model WRF,
Climate of the Past, 20, 449–465, https://doi.org/10.5194/cp-20-449-2024, 2024.

1838   Rybak, O. and Huybrechts, P.: A comparison of Eulerian and Lagrangian methods for dating in numerical ice-
sheet models, Ann. Glaciol., 37, 150–158, https://doi.org/10.3189/172756403781815393, 2003.

1840   Scherler, D. and Egholm, D. L.: Production and Transport of Supraglacial Debris: Insights From Cosmogenic
10Be and Numerical Modeling, Chhota Shigri Glacier, Indian Himalaya, J. Geophys. Res. Earth Surf., 125,
1842   https://doi.org/10.1029/2020JF005586, 2020.

1844   Schoof, C. and Hewitt, I.: Ice-Sheet Dynamics, Annu. Rev. Fluid Mech., 45, 217–239,
https://doi.org/10.1146/annurev-fluid-011212-140632, 2013.

1846   Seguinot, J. and Delaney, I.: Last-glacial-cycle glacier erosion potential in the Alps, Earth Surface Dynamics, 9,
923–935, https://doi.org/10.5194/esurf-9-923-2021, 2021.

1848   Seguinot, J., Ivy-Ochs, S., Jouvet, G., Huss, M., Funk, M., and Preusser, F.: Modelling last glacial cycle ice
dynamics in the Alps, Cryosphere, 12, 3265–3285, https://doi.org/10.5194/tc-12-3265-2018, 2018.

1850   Small, R. J., Clark, M. J., and Cawse, T. J. P.: The Formation of Medial Moraines on Alpine Glaciers, Journal of
Glaciology, 22, 43–52, https://doi.org/10.3189/S0022143000014040, 1979.

1852   Sugden, David. E. and John, Brian. S.: Glaciers and Landscape: A Geomorphological Approach, 1st ed., Edward
Arnold, London, 1–376 pp., 1976.

1854   Tadono, T., Ishida, H., Oda, F., Naito, S., Minakawa, K., and Iwamoto, H.: Precise Global DEM Generation by
ALOS PRISM, ISPRS Annals of the Photogrammetry, Remote Sensing and Spatial Information Sciences, II–4,
71–76, https://doi.org/10.5194/isprsannals-II-4-71-2014, 2014.

1856   Valla, P. G., Shuster, D. L., and van der Beek, P. A.: Significant increase in relief of the European Alps during
mid-Pleistocene glaciations, Nat. Geosci., 4, 688–692, https://doi.org/10.1038/ngeo1242, 2011.

1858   Veness, R. L., Clark, C. D., Ely, J. C., Knight, J. L., Igneczi, A., and Bradley, S. L.: Modelling erratic dispersal
accounting for shifting ice flow geometries: A new method and explanations of erratic dispersal of the British–
1860   Irish Ice Sheet, J. Quat. Sci., https://doi.org/10.1002/jqs.3720, 2025.

Venetz, I.: Sur l'ancienne extension des glaciers et sur leur retraite dans leur limites actuelles, in: Actes de la
1862   Société Helvétique des Sciences Naturelles. Quinzieme Réunion Annuelle à l'Hospice du Grand-Saint-Bernard,
21–22, 1830.

1864   Walder, J. S. and Fowler, A.: Channelized subglacial drainage over a deformable bed, Journal of Glaciology, 40,
3–15, https://doi.org/10.3189/S0022143000003750, 1994.

1866   Wang, B., Wald, I., Morrical, N., Usher, W., Mu, L., Thompson, K., and Hughes, R.: An GPU-accelerated particle
tracking method for Eulerian–Lagrangian simulations using hardware ray tracing cores, Comput. Phys. Commun.,
1868   271, 108221, https://doi.org/10.1016/j.cpc.2021.108221, 2022.

Wickert, A. D.: Open-source modular solutions for flexural isostasy: gFlex v1.0, Geoscientific Model
1870   Development Discussions, 8, 4245–4292, https://doi.org/10.5194/gmdd-8-4245-2015, 2015.

Wüthrich, L., Morabito, E. G., Zech, J., Trauerstein, M., Veit, H., Gnägi, C., Merchel, S., Scharf, A., Rugel, G.,
1872   Christl, M., and Zech, R.: 10Be surface exposure dating of the last deglaciation in the Aare Valley, Switzerland,
Swiss J. Geosci., 111, 295–303, https://doi.org/10.1007/s00015-018-0298-3, 2018.

1874   Zhang, T., Li, D., East, A. E., Walling, D. E., Lane, S., Overeem, I., Beylich, A. A., Koppes, M., and Lu, X.:
Warming-driven erosion and sediment transport in cold regions, Nat. Rev. Earth Environ., 3, 832–851,
1876   https://doi.org/10.1038/s43017-022-00362-0, 2022.